Scientific Research Publishing

Open Journal of Geology, 2026, 16(11), 791-831
https://www.scirp.org/journal/ojg
ISSN Online: 2161-7589
ISSN Print: 2161-7570

Petrographic and Geochemical Characterization of Type-A Granites in the Djember Massif North of Korbol (Southern Chad): Geodynamic Implications

Mahamat Boka Ramadane[1*], Doumnang Mbaïgane Jean-Claude[2], Madjimbe Guiguindibaye[1]

[1]Department of Biology and Geology, Sarh University, Sarh, Chad
[2]Laboratory of Geology, Geomorphology and Remote Sensing, University of N'Djamena, N'Djamena, Chad
Email: *bokaramadanemahamat2@gmail.com

How to cite this paper: Ramadane, M.B., Jean-Claude, D.M. and Guiguindibaye, M. (2026) Petrographic and Geochemical Characterization of Type-A Granites in the Djember Massif North of Korbol (Southern Chad): Geodynamic Implications. *Open Journal of Geology*, **16**, 791-831.
https://doi.org/10.4236/ojg.2026.1611038

Received: June 25, 2026
Accepted: November 16, 2026
Published: November 19, 2026

Copyright © 2026 by author(s) and Scientific Research Publishing Inc.
This work is licensed under the Creative Commons Attribution International License (CC BY 4.0).
http://creativecommons.org/licenses/by/4.0/

Open Access

Abstract

Due to the presence of laterite and sedimentary cover, as well as the geographical isolation of the study area, the Precambrian basement in the southern part of the Saharan metacraton (Central Africa) remains largely unknown. Here we present granites from the Djember Massif north of Korbol (southern Chad), which have provided a better understanding of the nature of the local basement in this area. Two distinct petrographic types are described: an amphibole-biotite granite and a biotite granite. These granites are presented with the aim of constraining the origin and petrogenesis of type-A magmatism in the Central African orogenic belt, south of the Saharan Metacraton. The study area consists of biotite granite and biotite-amphibole granite. The geochemistry of these granites reveals a hyper-K syenogranitic composition, rich in SiO_2 (68% - 78%), and low in P_2O_5 (<0.5%). The biotite granite is slightly hyperaluminous and strongly fractionated calc-alkaline to calc-alkaline, while the biotite-amphibole granite is alkaline to calc-alkaline and metaluminous to slightly hyperaluminous. Biotite granite is Type I and represents a transitional form between biotite and amphibole granites. The chondrite-normalized REE profiles show significant enrichment in LREE, pronounced negative anomalies in Eu (EuN/Eu*: 0.36 - 0.50 in biotite granite; 0.41 - 0.57 in biotite-amphibole granite), and positive Eu anomalies of varying magnitudes (EuN/Eu*: 1.31 and 6.24 in biotite granite). These granites exhibit the typical geochemical characteristics of Type-A granites and belong to the family of oxidized Type-A granites. The analyzed granites are thought to have derived from the partial melting of a heterogeneous crustal source consisting of immature (meta)grauwackes and detritus of quartz-feldspar igneous rocks derived from continental

arcs, consistent with crustal delamination induced by plate rupture leading to subduction of mantle magma, during the post-collisional Pan-African phase. These magmas would then have evolved through fractional crystallization controlled by alkali feldspar within the upper continental crust. These results highlight the role of crustal thinning and delamination in the genesis of type-A magmas in the Guéra Massif and contribute to the understanding of the tectonomagmatic evolution of the Central African orogenic belt south of Chad.

Keywords

Type-A Granites, Djember Massif, Post-Collisional Magmatism, Central African Orogenic Belt, Southern Chad

1. Introduction

The Pan-African rock units of the basement located north of Korbol are very poorly documented. The study area lies south of the Sahara metacraton (**Figure 1**) and was formed during the Neoproterozoic Pan-African orogeny [1]. This refers to the Trans-Saharan orogen, the East African orogen, and the Oubangides [1]-[8]. These mobile belts are highly deformed crustal segments resulting from the amalgamation of reworked microcratonic domains and juvenile crust (extracted from the mantle shortly before its incorporation into the belts). The juvenile crust formed between 0.8 and 0.65 Ga, during the closure of several oceanic domains, and encompasses a range of (meta)igneous and (meta)sedimentary rocks that collectively represent remnants of active margins [9]-[12]. The inherently composite nature of mobile belts is more clearly illustrated by the varied radiogenic isotopic signature of their Upper Neoproterozoic igneous rocks, which indicates the incorporation of two distinct geochemical reservoirs: an ancient basement (Neoarchean to Paleoproterozoic cratonic fragments) and Neoproterozoic arc rocks [11] [13]-[15]. The Arabo-Nubian Shield, located within the East African Orogen (**Figure 2**), represents a remarkable anomaly, as there is no evidence of a pre-Neoproterozoic crust [16]. These mobile belts also contain significant volumes of post-collisional igneous rocks and have been dissected by continent-scale shear zones (hundreds of kilometers long) that can be traced into the adjacent South American continent [17]-[19]. The northern Korbol sector is located in a critical zone at the southern margin of the Saharan metacraton and within the so-called Ouban guides or Central African orogenic belt, which connects it to the Congo craton [1] [19] [20]. Granitoids make up the bulk of the continents [21]. They also exhibit a great deal of diversity in terms of petrogenesis and geochemistry. This diversity has been used to determine their origin, genesis, and development in relation to the geodynamic environment in which they formed and were emplaced [22] [23]. The Guéra Massif, located in central Chad, exposes the Precambrian basement, which is part of the Pan-African orogenic belt of Central Africa (see **Figure 1**). This belt separates the

Congo Craton to the south, the West African Craton to the west, and the Saharan Metacraton to the north [1] [2] [7] [24]. It consists of a Neoproterozoic juvenile crust composed of granitoids and enclaves [25]-[27].

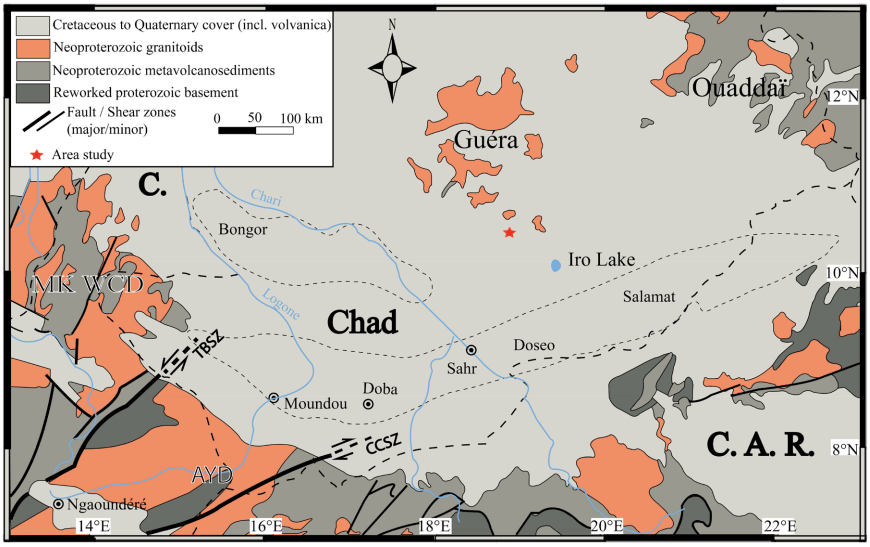


Figure 1. Geological map of southern Chad and adjacent countries. The map was redrawn and adapted from the geological map of Africa at a scale of 1/10,000,000 [28]. Dotted lines depict the outlines of the Cretaceous-Tertiary rift basins in southern Chad (redrawn from [29]). Abbreviations: C.A.R., Central African Republic; C., Cameroon; MK-WCD, Mayo Kebbi-West Cameroon domain, AYD, Adamawa-Yadé domain, TBSZ, Tcholliré-Banyo shear zone; CCSZ, Central Cameroon shear zone.

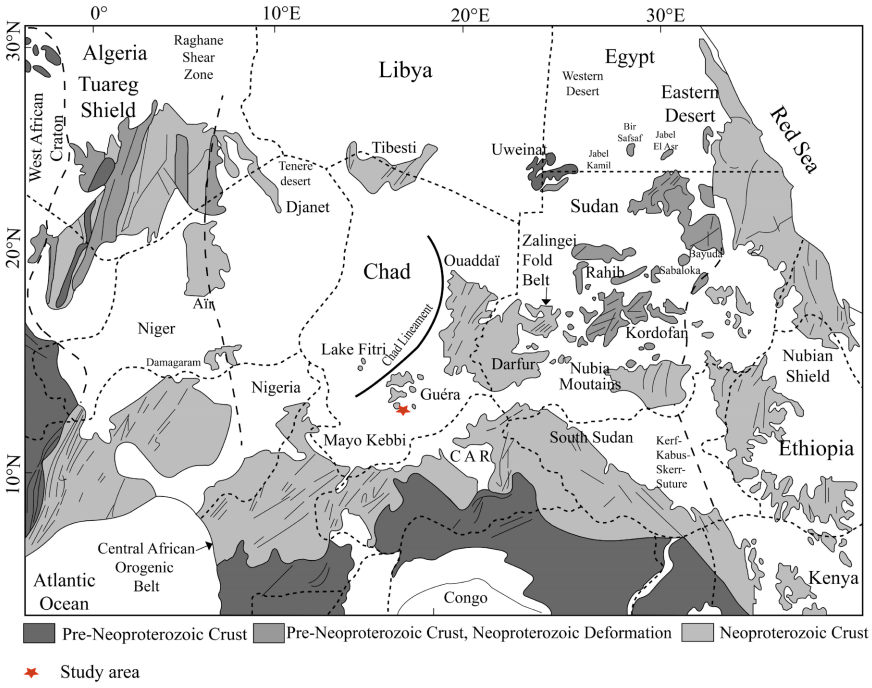


Figure 2. Regional geological framework map of North-Central Africa showing the boundaries of the Saharan Metacraton and the Neoproterozoic massifs that comprise Chad and the surrounding region (modified from [1]).

However, the geology of the S-SE region of Chad is relatively poorly understood due to its geographic isolation and the extensive presence of laterite and recent sedimentary cover.

2. Geological Setting

In Chad, the basement formations are distributed in the north in the Tibesti Massif, in the east in the Ouaddaï Massif, in the southwest in the Mayo Kebbi Massif, in the center in the Guéra Massif (**Figure 2**), and in the south in the Yadé Massif, also known as the Baïbokoum Massif. The Guéra Massif is a complex composed of amphibole-bearing monzonitic granite (Abou Déïa type) or highly radioactive alkaline leucocratic granite [30]-[35]. The metamorphic formations of the Guéra include the metavolcanic-sedimentary series, which are often found as enclaves within the granite and are associated with the Goz Beïda Group [30] [32]. Datings of granites near Lake Fitri are presumed to be Neoproterozoic in age. New U/Pb zircon geochronology of granitic rocks from the Guéra Massif, the Lake Fitri region, and the Doba Basin in southern Chad has yielded weighted-average 206Pb/238U ages ranging from 595 ± 8 Ma to 545 ± 6 Ma [36]. Thus, in the Lake Iro area, porphyritic granites yield U-Pb zircon formation ages corresponding to a period ranging from 575.3 ± 5.6 to 581.3 ± 3.8 Ma [37]. The Yadé Massif, also known as the Baïbokoum Massif, is located on Chad's southern border and extends into the Central African Republic and Cameroon. It is characterized by an abundance of syn-tectonic granitoids containing enclaves of metamorphic rocks cut by late granitic intrusions [38]-[42]. This Yadé massif includes Neoproterozoic ages, notably a granite and a syenite described by [43] and [44], which yielded K-Ar and Rb-Sr ages on whole rock ranging from 632 to 568 Ma. The Ouaddaï Massif is composed of metasedimentary sequences, containing mafic magmatic intercalations in the form of amphibolite [30] [45] [46]. The age of the hyperaluminous granites was constrained by U-Pb dating of zircon, yielding 635 ± 3 Ma for a biotite leucogranite and 613 ± 8 Ma for a muscovite and garnet leucogranite. The age of the metaluminous, calc-alkaline, and strongly potassic to shoshonitic series was determined to be 540 ± 5 Ma by U-Pb dating of zircons from a biotite granite [34] [35] [44] [46]. The Mayo-Kébbi domain is an elongated structure extending in a NE-SW direction, located between the Central Cameroon and Northern Cameroon domains. It differs from these two domains in that it consists of a young Neoproterozoic crust [26] [27] [47] [48]. This domain corresponds to a magmatic arc zone that formed between 800 Ma and 550 Ma through successive collisions with the Central Cameroon and Northern Cameroon domains, respectively [26] [27] [47]. It comprises the greenstone belts, the Mayo-Kébbi batholith, and post-tectonic intrusions [25]-[27] [30] [47]-[49]. The Tibesti Massif consists of metasedimentary rocks and metavolcanic rocks [50] and a suite of granoblastic, locally migmatitic amphibolites associated with various gneisses and granitoids. Ages ranging from 1250 to 820 Ma have been obtained for the Lower Tibestian [51]. The Upper Tibestian consists of weakly metamorphosed detrital rocks [30]. Various

calc-alkaline intrusions dated between 600 and 530 Ma (Super-Tibestian magmatic series and the Ben Ghnema batholith, Eghei magmatic series, and the Wadi Yebigue pluton) cut through the Lower and Upper Tibestian formations [51] [52].

3. Methodology

The different petrographic types identified following the field surveys are biotite granite and biotite-amphibole granite. A total of 17 samples were selected, including six (6) samples of biotite granite and eleven (11) samples of biotite-amphibole granite. Analyses were conducted on the chemical composition of the whole rock using ICP-AES techniques. This method made it possible to assess the major components and several trace elements present in the samples. All analyses were performed at the ALS Geochemistry laboratory in Johannesburg, South Africa, which is equipped with an inductively coupled plasma atomic emission spectrometer (ICP-AES). Comprehensive chemical analyses of the rocks were performed, and the results are presented in Table 1. Table 1 provides information on the major and trace elements extracted from outcrops located north of Korbol. The major element analysis was performed using inductively coupled plasma atomic emission spectrometry (ICP-AES); 0.2 g of rock powder was fused with 1.5 g of $LiBO_2$ and then dissolved in 100 mm of 35% HNO_3. The concentrations of trace elements and rare earth elements (REEs) were determined by ICP-MS from slurries obtained after dissolving 0.25 g of rock powder using four acid digestions. Analytical accuracies range from 0.1% to 0.02% for major elements, from 0.01 to 0.5 ppm for trace elements, and from 0.01 to 5 ppm for rare earth elements.

Table 1. Abundances of major elements in the granites of the Djember Massif.

Sample	MB44	MB54	MB64	MB46	MB05	MB50	MB47	MB12	MB42	MB43	MB01	MB18	MB03	MB58	MB08	MB56	MB10
Rock type	BGr	BGr	BGr	BGr	BGr	BGr	BHGr	BHGr	BHGr	BHGr	BHGr	BHGr	BHGr	BHGr	BHGr	BHGr	BHGr
SiO_2 (wt.%)	71.6	74.4	74.5	74.6	77.4	73.2	74.5	70.5	73.5	75.8	74.2	72.3	71.3	69.1	69.1	68.6	69.2
Al_2O_3	14.15	13.45	13.25	13.75	12.9	12.65	12.85	15.45	12.95	12.55	13.95	14.55	14.4	14.6	15.2	14.75	15.5
Fe_2O_3t	1.76	2.05	1.92	1.02	0.65	3.43	3.05	2.95	2.98	3.03	1.7	2.53	2.68	3.54	3.31	3.68	3.56
CaO	1.15	0.83	0.76	0.74	0.54	1.28	0.93	1.47	0.67	1.12	0.75	1.05	1.02	1.33	1.21	1.4	1.34
MgO	0.26	0.2	0.26	0.09	0.01	0.32	0.28	0.46	0.38	0.22	0.19	0.35	0.36	0.61	0.52	0.61	0.58
Na_2O	3.46	3.3	3.42	3.73	3.34	2.95	2.79	4.44	2.52	2.92	3.71	3.89	3.95	3.92	4.28	4.16	4.22
K_2O	5.28	5.3	5.56	5.19	5.3	4.84	5.47	5.08	6.32	4.84	5.61	5.69	5.67	5.84	5.78	5.62	6.08
TiO_2	0.18	0.19	0.23	0.08	0.03	0.31	0.29	0.47	0.28	0.26	0.26	0.39	0.41	0.65	0.53	0.66	0.64
MnO	0.04	0.07	0.06	0.05	0.01	0.08	0.07	0.06	0.07	0.08	0.03	0.06	0.07	0.08	0.09	0.09	0.09
P_2O_5	0.05	0.04	0.12	0.01	-	0.06	0.04	0.12	0.04	0.04	0.04	0.08	0.09	0.13	0.11	0.16	0.13
LOI	0.45	0.49	0.73	0.41	0.29	0.7	0.7	0.59	0.42	0.52	0.36	0.34	0.44	0.57	0.52	0.56	0.4

Continued

Sum	97.93	99.83	100.08	99.26	100.18	99.12	100.27	101	99.71	100.86	100.44	100.89	99.95	99.8	100.13	99.73	101.34
$Na_2O + K_2O$	8.92	8.61	8.97	8.99	8.62	7.86	8.24	9.43	8.87	7.69	9.28	9.50	9.62	9.78	10.05	9.81	10.16
K_2O/Na_2O	1.53	1.61	1.63	1.39	1.59	1.64	1.96	1.14	2.51	1.66	1.51	1.46	1.44	1.49	1.35	1.35	1.44
Al_2O_3/TiO_2	78.61	70.79	57.61	171.88	430	40.81	44.31	32.87	46.25	48.27	53.65	37.31	35.12	22.46	28.68	22.35	24.22
Di														0.72	0.14	0.88	0.41
Cor	0.78	0.86	0.48	0.68	0.69	0.36	0.73	0.23	0.84	0.55	0.50	0.25	0.10				
DI	90.21	91.53	92.62	93.84	95.66	87.43	89.53	87.41	90.53	89.00	92.92	90.19	90.17	87.41	88.15	87.05	87.38
Mg#	27.10	19.71	25.41	18.17	3.73	19.01	18.76	28.18	24.29	15.45	21.95	25.82	25.26	30.24	28.33	29.43	29.07
A/NK	1.24	1.20	1.14	1.17	1.15	1.25	1.22	1.21	1.18	1.25	1.15	1.16	1.14	1.14	1.14	1.14	1.15
A/CNK	1.05	1.06	1.02	1.05	1.06	1.02	1.05	1.00	1.06	1.04	1.03	1.01	0.99	0.96	0.98	0.95	0.97
CCPI	17.42	19.21	18.12	10.15	6.44	30.42	26.80	24.65	25.72	27.52	15.58	21.52	22.37	28.00	25.80	28.62	26.86
AI	54.58	57.11	58.20	54.15	57.78	54.95	60.72	48.38	67.75	55.60	56.53	55.01	54.82	55.13	53.44	52.84	54.50

LOI: Loss on Ignition; Di: standard diopside; Cor: standard corundum; DI: Differentiation Index (DI = sum of normative Qz + Or + Ab); A/NK: molar $Al_2O_3/(Na_2O + K_2O)$; A/CNK: molar $Al_2O_3/(CaO + Na_2O + K_2O)$; Mg#: magnesium number (molar MgO/(MgO + FeO)); CCPI: chlorite-carbonate-pyrite index; AI: alteration index ([57]); Fe_2O_3t = total iron as Fe^{3+}; - = below detection limit; BGr = biotite granite; BHGr = biotite and amphibole granite.

4. Results

4.1. Field Description and Petrography

The Korbol region in southern Chad comprises the Djember Massif, consisting of granites, gabbro, diorite, and quartz syenite, containing in places amphibolite enclaves (biotite and pyroxene) and xenoliths of biotite gneiss. The granites, which are the subject of this study, form the majority of the Djember Massif (**Figure 3**). They are subdivided into biotite granite (BGr), biotite-amphibole granite (BHGr), and garnet granite (GGr). The GGr was not subjected to whole-rock geochemical analyses.

4.1.1. Biotite Granite

Biotite granite (BGr) is the second most abundant petrographic type in the Djember Massif, outcropping as slabs and boulders (**Figure 4(a)**), with amphibolite inclusions and xenoliths of biotite gneiss of varying sizes. The texture is porphyroid-grained with minerals ≤ 4 mm in size. The major mineral phases of the rock include sub-tabular crystals of potassium feldspars (30% - 40% by vol.), represented mainly by microcline and secondarily by orthoclase exhibiting perthitic exsolutions (**Figure 4(b)**), quartz ocelli, fractures sealed by quartz or biotite, inclusions (biotite, plagioclase, and opaque minerals), or localized sericite alteration; xenomorphic quartz crystals (20% - 30% vol.), exhibiting weak undulating extinction and inclusions of biotite, titanite, and opaque minerals. Other major minerals include sub-tabular plagioclase crystals (15% - 18% vol.) exhibiting myrmekitic or

graphic textures associated with concentric zoning (Figure 4(c)), kink-band deformation, microfractures sealed by quartz or potassium feldspar, and alteration to damourite and epidote; and sub-automorphic biotite flakes (5% - 8% by vol.) exhibiting inclusions of titanite, zircon, or opaque minerals, and chlorite alteration. The accessory phases consist of apatite, zircon, titanite (which regularly forms a retrograde ring around the opaque minerals, *i.e.*, an atoll microstructure; Figure 4(d)), and opaque minerals.

4.1.2. Biotite- and Amphibole-Bearing Granite

BHGr is the most abundant petrographic type in the Djember Massif. It outcrops as slabs (Figure 4(e)) and blocks, with a massive structure composed of fine and coarse grains. Under the microscope, BHGr exhibits a porphyroid granular texture. Potassium feldspar (30% - 40%. vol.) forms tabular to sub-tabular crystals of microcline or orthoclase exhibiting orthoclase-microcline inversion, perthitic textures (Figure 4(f)), and inclusions of biotite, plagioclase, apatite, zircon, titanite, opaque minerals, and quartz ocelli; however, fractures filled with quartz or plagioclase, and sericite alteration are observed. Quartz (20% - 25% by volume) forms xenomorphic crystals that sporadically exhibit undulating extinction or a checkerboard structure, along with inclusions of alkali feldspar, plagioclase, biotite, tures (Figure 4(g)), and inclusions of biotite, potassium feldspar, green crystals

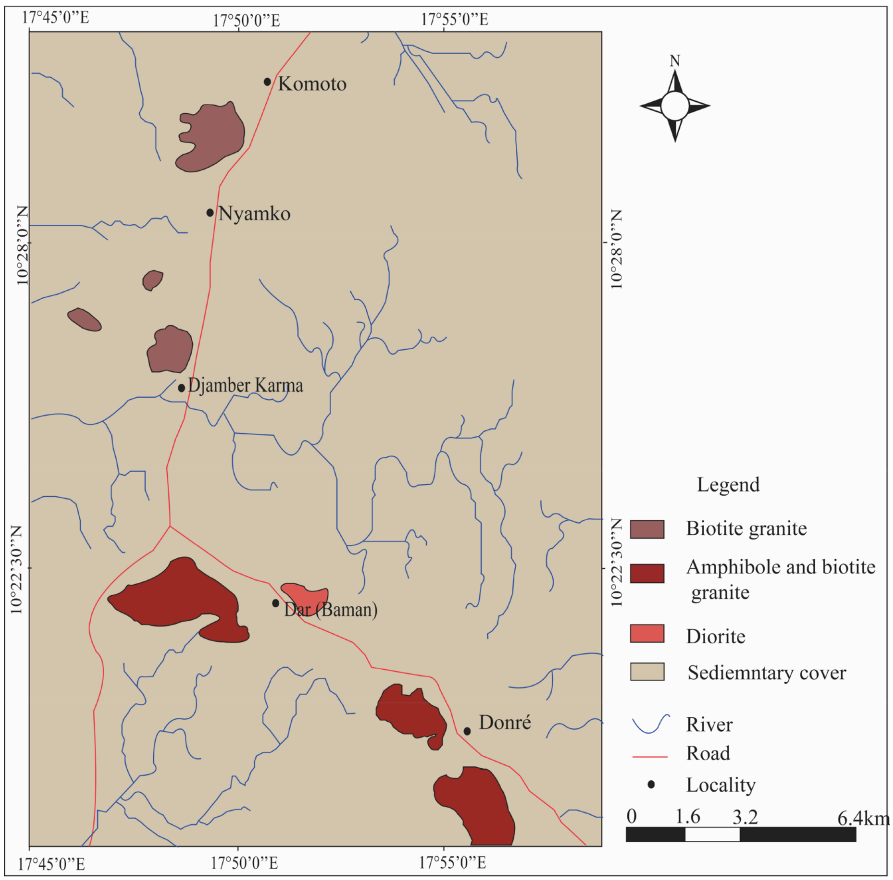


Figure 3. The geological map of the study area.

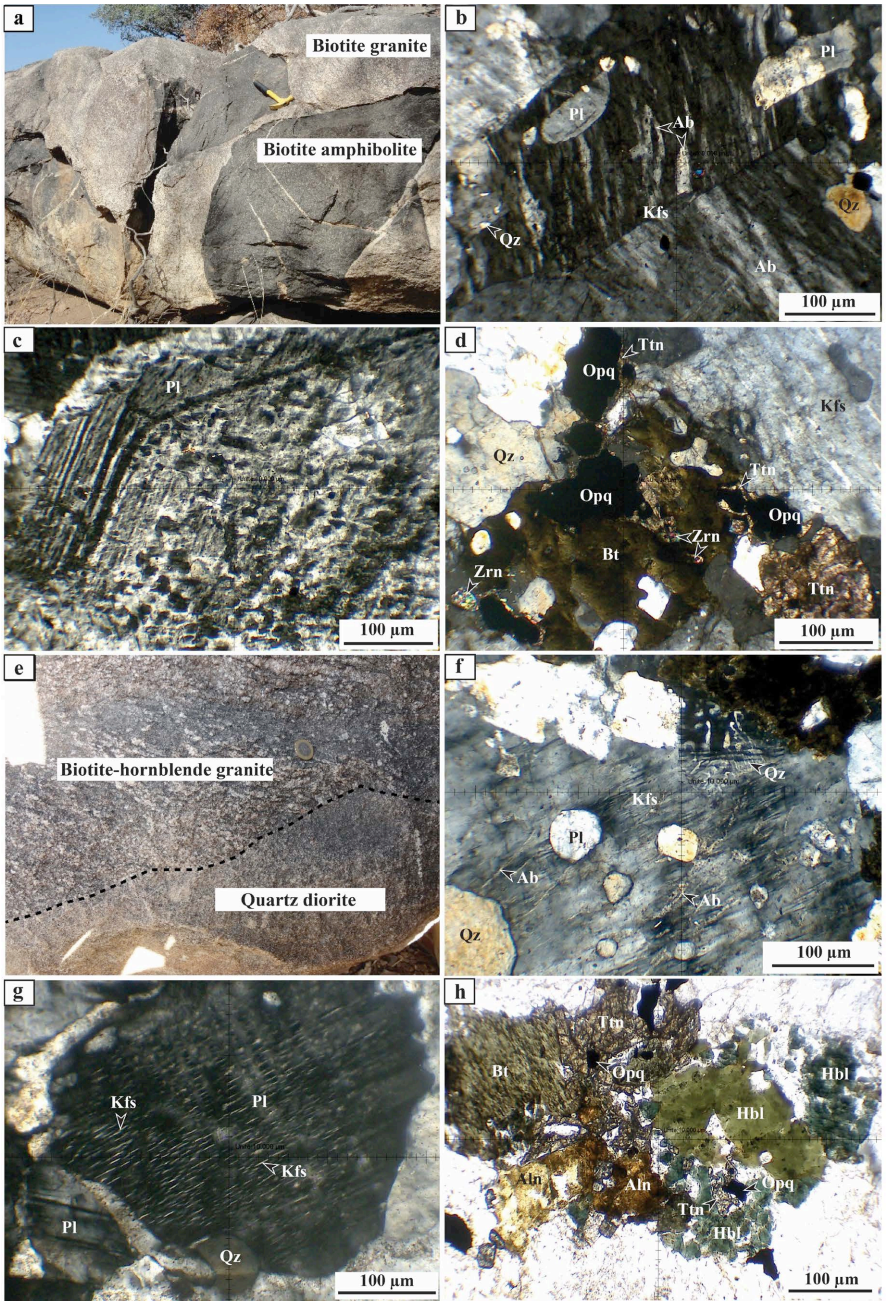


Figure 4. Photographs (a and e) and LPA and LPNA microphotographs of biotite granite (a, b, c, and d) and biotite-amphibole granite (e, f, g, and h). (a) Block containing biotite amphibolite enclaves; (b) Perthite-type albite exsolutions in a Carlsbad-twinned orthoclase crystal; (c) Graphic texture associated with concentric zoning in a plagioclase crystal; (d) Biotite flake containing zircon inclusions and associated with titanite crystals; (e) Slab of biotite- and amphibole-bearing granite showing a sharp contact with the quartz diorite at the margin; (f) Perthite-type albite exsolutions in a potassium feldspar crystal; (g) Potassium feldspar exsolutions in a plagioclase crystal; (h) Green hornblende crystals associated with titanite, allanite, opaque minerals, and biotite crystals.

amphibole, apatite, zircon, and opaque minerals. The sub-rectangular plagioclase (10% - 15% by volume) exhibit synneusis, myrmekitic or anti-perthitic texhorn-

blende, apatite, opaque minerals, and quartz ocelles. In addition, the plagioclase is zoned, with tectonic twinning or microfractures filled with quartz, biotite, or green hornblende, and alteration to damourite and epidote. The biotite lamellae (8% - 10% by volume) contain inclusions of zircon, allanite, titanite, or opaque minerals, and sometimes show chlorite transformation. The amphibole is a green hornblende (3% - 5% by volume) forming sub-rectangular or moderately prismatic sections, with inclusions of apatite, zircon, titanite, and opaque minerals. Accessory minerals include opaque minerals (surrounded by a retrograde halo of titanite grains), titanite, zircon, apatite, and allanite (**Figure 4(h)**).

4.2. Whole-Rock Geochemistry

Whole-rock geochemical data for seventeen representative samples including 6 samples of biotite granite and 11 samples of biotite-amphibole granite are presented in **Tables 1-3**.

Table 2. Trace element abundances in the granites of the Djember Massif.

Sample	MB44	MB54	MB64	MB46	MB05	MB50	MB47	MB12	MB42	MB43	MB01	MB18	MB03	MB58	MB08	MB56	MB10
Rock type	BGr	BGr	BGr	BGr	BGr	BGr	BHGr	BHGr	BHGr	BHGr	BHGr	BHGr	BHGr	BHGr	BHGr	BHGr	BHGr
Ba (ppm)	1095	680	446	314	607	1105	1090	970	1205	1225	452	584	563	1045	1080	1085	1155
Cr	135	144	131	113	195	131	169	104	88	119	120	83	133	119	115	98	107
Cs	3.34	7.21	1.44	5.11	0.42	6.06	6.22	0.54	5.38	2.82	0.45	0.79	1.82	1.99	8.21	1.78	2.64
Ga	24.4	25.4	23.2	23.6	20.2	27.7	30	21.7	26.4	25.4	21.9	21.4	20.6	22.8	24.3	24.2	25.3
Hf	3.61	6.72	8.84	4.16	1.19	12.15	9.53	14.4	10.7	11.45	8.95	11.05	10.4	16.35	14.85	15.85	15.1
Nb	13	23.9	22.8	23.4	1.32	29.2	29.6	18.65	41.2	24.9	10.15	20.3	21.1	34	28.8	37.5	33
Rb	209	231	208	197	133	215	246	121	273	183	153	185.5	163	189.5	196.5	193.5	205
Sc	2.6	4.7	0.7	3.3	-	12.3	4.4	5.3	7.5	11	1.7	5	5.3	6	6.5	4.3	8.1
Sn	2.8	4	1.8	2.2	0.6	7.8	6.1	1.5	2.8	5.2	1.2	1.6	2.4	3.5	4.5	3.6	3.9
Sr	174	98.7	100.5	123.5	144	90.5	91.2	214	79.8	92.3	99.7	131	112	164	159.5	164	173.5
Ta	0.7	1.5	1.1	1.5	0.1	2	1.5	1	1.9	1.1	0.5	1	1.1	1.9	1.8	2.4	2
Th	6.55	15.05	32.2	8.59	2.05	27	22.7	26	28.6	28.7	23.1	29.2	17.75	23.7	56.3	18.2	24.2
U	1.89	1.94	3.31	5.51	1	2.36	1.93	2.12	3.86	2.09	2.39	2.48	2.36	2.97	5.79	2.82	3.57
V	12	7	7	-	-	13	11	19	8	10	5	11	12	21	18	19	21
W	-	0.5	1	0.7	-	0.7	0.8	0.6	0.7	0.7	-	-	0.5	1	1.5	1.1	0.7
Y	23.4	40.4	20.7	24.8	2	119.5	88.1	32.4	88.4	104.5	15.2	32.1	36.2	35	50.7	41.4	45.3
Zr	122	203	321	102	35	355	315	644	343	369	352	455	438	716	671	691	696
Co	2	2	2	1	1	3	3	3	2	2	2	2	2	3	2	2	3
Cu	1	1	1	1	10	-	4	1	1	4	-	1	1	2	2	3	3
Li	30	30	10	20	-	40	50	20	40	30	10	10	10	20	20	20	20
Mo	-	1	2	1	6	1	1	2	1	2	1	2	3	2	2	3	2
Ni	3	2	3	1	2	3	3	2	2	2	2	1	2	1	2	2	2

Continued

Pb	44	46	25	43	24	38	44	27	43	36	27	30	24	23	30	27	29
Sc	2	4	1	3	-	10	4	5	7	10	2	4	4	6	5	6	7
Zn	88	97	52	42	4	172	164	68	167	145	39	67	69	105	93	110	95
Rb/Sr	1.20	2.34	2.07	1.60	0.92	2.38	2.70	0.57	3.42	1.98	1.53	1.42	1.46	1.16	1.23	1.18	1.18
Zr/Hf	33.80	30.21	36.31	24.52	29.41	29.22	33.05	44.72	32.06	32.23	39.33	41.18	42.12	43.79	45.19	43.60	46.09
Sr/Y	7.44	2.44	4.86	4.98	72.00	0.76	1.04	6.60	0.90	0.88	6.56	4.08	3.09	4.69	3.15	3.96	3.83
Th/La	0.37	0.50	0.39	1.28	0.11	0.26	0.31	0.33	0.42	0.32	0.35	0.35	0.19	0.16	0.21	0.13	0.18
Ba/Rb	5.24	2.94	2.14	1.59	4.56	5.14	4.43	8.02	4.41	6.69	2.95	3.15	3.45	5.51	5.50	5.61	5.63
Y/Nb	1.80	1.69	0.91	1.06	1.52	4.09	2.98	1.74	2.15	4.20	1.50	1.58	1.72	1.03	1.76	1.10	1.37

Table 3. Abundances of rare earth elements in the granites of the Djember Massif.

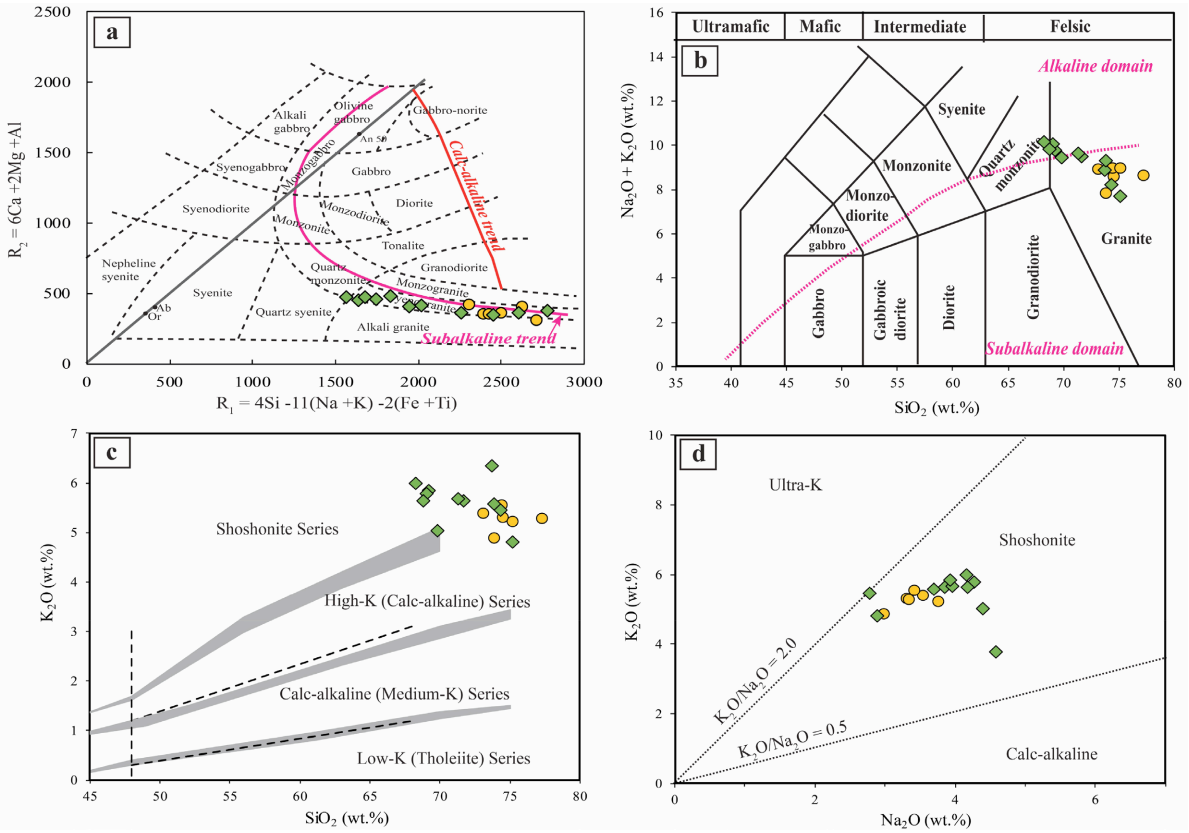
Sample	MB44	MB54	MB64	MB46	MB05	MB50	MB47	MB12	MB42	MB43	MB01	MB18	MB03	MB58	MB08	MB56	MB10
Rock type	BGr	BGr	BGr	BGr	BGr	BGr	BHGr	BHGr	BHGr	BHGr	BHGr	BHGr	BHGr	BHGr	BHGr	BHGr	BHGr
La (ppm)	17.8	30	83.5	6.7	19.2	105.5	73.2	79.2	68.9	91.1	66.5	83.8	94	149.5	263	135.5	137
Ce	36.5	81.4	164	16.6	14.8	218	147.5	162.5	140.5	198	146.5	190.5	163.5	297	382	281	272
Pr	4.28	8.39	17.1	1.98	1.62	29.5	18.6	17.8	16.95	23.2	13.35	19.2	18.55	30.6	36.1	30.6	29.2
Nd	16.6	32.8	58.8	8.6	5	116	74.1	62.8	69.4	94.3	46	69	66	105	116.5	103	103.5
Sm	3.43	7.87	8.72	3.19	0.57	24.6	16.6	10.85	15.25	21	7.13	11.25	10.95	15.8	16.15	17.2	17.05
Eu	1.51	1.24	0.83	0.46	0.95	3.17	2.47	1.7	2.54	2.97	0.97	1.28	1.62	2.22	2.25	2.13	2.33
Gd	3.6	7.28	5.63	3.44	0.38	24.6	15.25	7.63	14.95	20	4.57	7.98	8.01	11.45	11.4	11.6	11.35
Tb	0.56	1.26	0.7	0.65	0.05	4.07	2.37	1.06	2.29	3.04	0.61	1.16	1.02	1.42	1.54	1.52	1.53
Dy	3.69	7.49	3.43	4.49	0.29	24.7	14.75	6.05	14.5	19.25	3.12	6.04	5.67	7.22	8.16	8.36	8.39
Ho	0.79	1.44	0.64	0.93	0.05	4.51	2.89	1.1	3.02	3.76	0.57	1.14	1.08	1.4	1.58	1.54	1.55
Er	2.31	4.22	1.78	2.71	0.17	13.9	8.29	2.87	8.89	10.25	1.37	3.02	2.94	3.47	4.46	4.34	4.17
Tm	0.33	0.62	0.27	0.4	0.02	1.96	1.24	0.43	1.33	1.5	0.22	0.42	0.42	0.47	0.64	0.61	0.58
Yb	2.11	4.05	1.56	2.72	0.19	12.3	7.71	2.62	8.23	9.02	1.3	2.73	2.68	3.34	4.05	4.3	3.77
Lu	0.31	0.64	0.21	0.38	0.03	1.81	1.22	0.42	1.23	1.31	0.22	0.41	0.44	0.57	0.62	0.65	0.64
ΣREE	93.82	188.7	347.17	53.25	43.32	584.62	386.19	357.03	367.98	498.7	292.43	397.93	376.88	629.46	848.45	602.35	593.06
ΣLREE	80.12	161.7	332.95	37.53	42.14	496.77	332.47	334.85	313.54	430.57	280.45	375.03	354.62	600.12	816	569.43	561.08
ΣHREE	13.7	27	14.22	15.72	1.18	87.85	53.72	22.18	54.44	68.13	11.98	22.9	22.26	29.34	32.45	32.92	31.98
Sm/Nd	0.21	0.24	0.15	0.37	0.11	0.21	0.22	0.17	0.22	0.22	0.16	0.16	0.17	0.15	0.14	0.17	0.16
$(La/Lu)_N$	5.96	4.87	41.30	1.83	66.48	6.05	6.23	19.59	5.82	7.22	31.40	21.23	22.19	27.24	44.06	21.65	22.23
$(La/Sm)_N$	3.26	2.40	6.02	1.32	21.19	2.70	2.77	4.59	2.84	2.73	5.87	4.69	5.40	5.95	10.24	4.96	5.05
$(Gd/Lu)_N$	1.44	1.41	3.33	1.13	1.57	1.69	1.55	2.26	1.51	1.90	2.58	2.42	2.26	2.50	2.29	2.22	2.20
$(La/Yb)_N$	5.69	4.99	36.09	1.66	68.13	5.78	6.40	20.38	5.64	6.81	34.49	20.70	23.65	30.18	43.78	21.24	24.50
Ce_N/Ce^*	1.01	1.23	1.04	1.10	0.64	0.94	0.96	1.04	0.99	1.04	1.18	1.14	0.94	1.06	0.94	1.05	1.04
Eu_N/Eu^*	1.31	0.50	0.36	0.42	6.24	0.39	0.47	0.57	0.51	0.44	0.52	0.41	0.53	0.50	0.51	0.46	0.51

$EuN/Eu^* = EuN/(SmN^*GdN)^{1/2}$, $CeN/Ce^* = CeN/(LaN^*PrN)^{1/2}$, where N denotes normalization to the chondrite values.

4.2.1. Major Element Characteristics

SiO_2 abundances range from 73.11% to 77.26% in the BGr, and from 68.28% to 75.15% in the BHGr (**Table 1**). These granites exhibit high alkali contents (Na_2O + K_2O = 7.86% - 8.99% in the BGr, and 7.69% - 10.16% in the BHGr), and low CaO contents (0.54% - 1.46%). In the R1 - R2 multi-cation classification diagram [53], the analyzed samples follow the subalkaline trend and occupy primarily the syenogranite domain (**Figure 5(a)**). Accordingly, they occupy the granite domain and belong either exclusively to the subalkaline series (BGr) or straddle the alkaline and subalkaline domains (BHGr) in the Na_2O + K_2O vs. SiO_2 diagram (**Figure 5(b)**; [54]). Furthermore, when plotted on the K_2O vs. SiO_2 diagram (**Figure 5(c)**), these samples fall within the highly potassic calc-alkaline series with a shoshonitic tendency. They occupy primarily the shoshonitic rock domain, allowing them to be classified as "true shoshonites", for which K_2O/Na_2O ratios range from 0.5 to 2 (**Figure 5(d)**; [55]). Consistent with their high differentiation indices (DI), ranging from 87.05 to 95.66, the BGr is predominantly found in the highly fractionated calc-alkaline granite (HFCA) domain, while the BHGr is found primarily in the alkaline granite domain (**Figure 5(e)**). They exhibit predominantly calcic-alkaline and alkaline affinities, respectively, for the BGr and the BHGr (**Figure 5(f)**; [56]).

Furthermore, the analyzed granites exhibit lower MgO contents (0.01% - 0.61%) compared to FeOt (0.58% - 3.32%), which gives them a ferriferous affinity characteristic of Type-A granites, as illustrated in the FeOt/(FeOt + MgO) vs. SiO_2 diagram (**Figure 5(g)**; [56]). In the (molar %) A/NK vs. A/CNK diagram (**Figure 5(h)**;



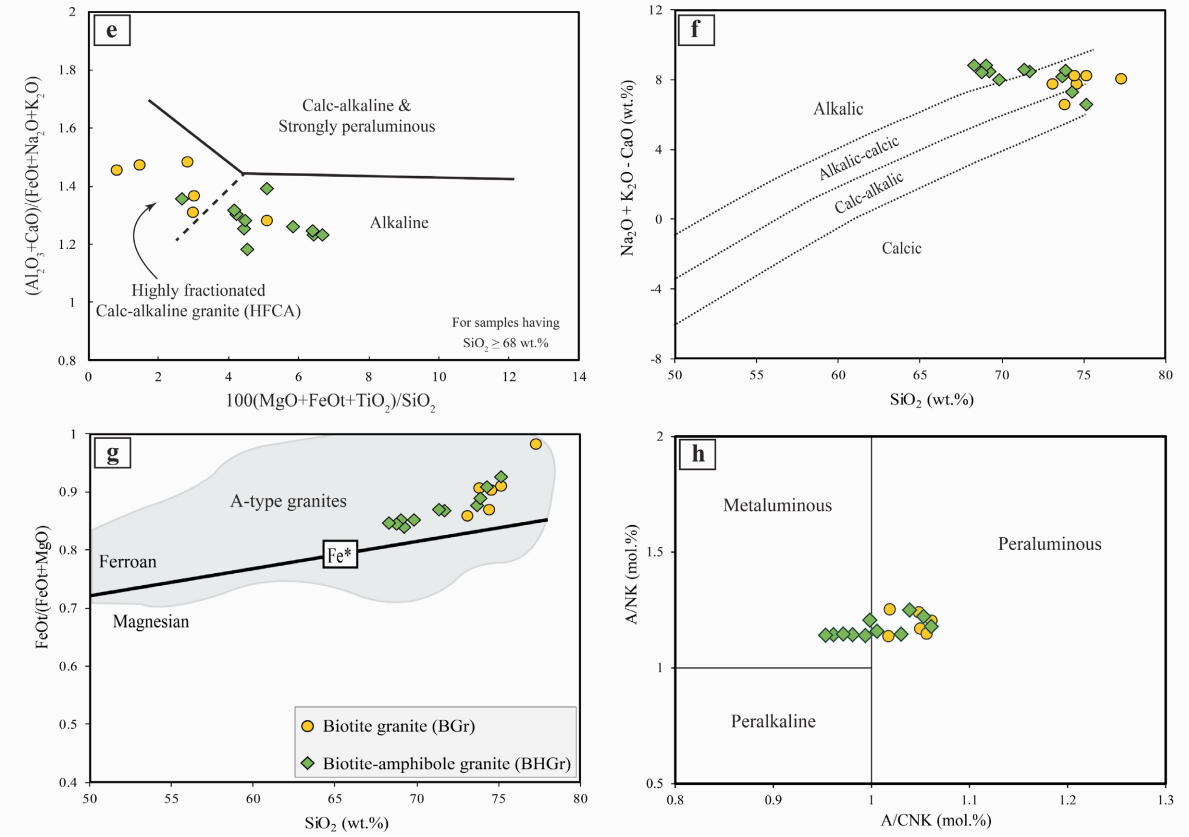


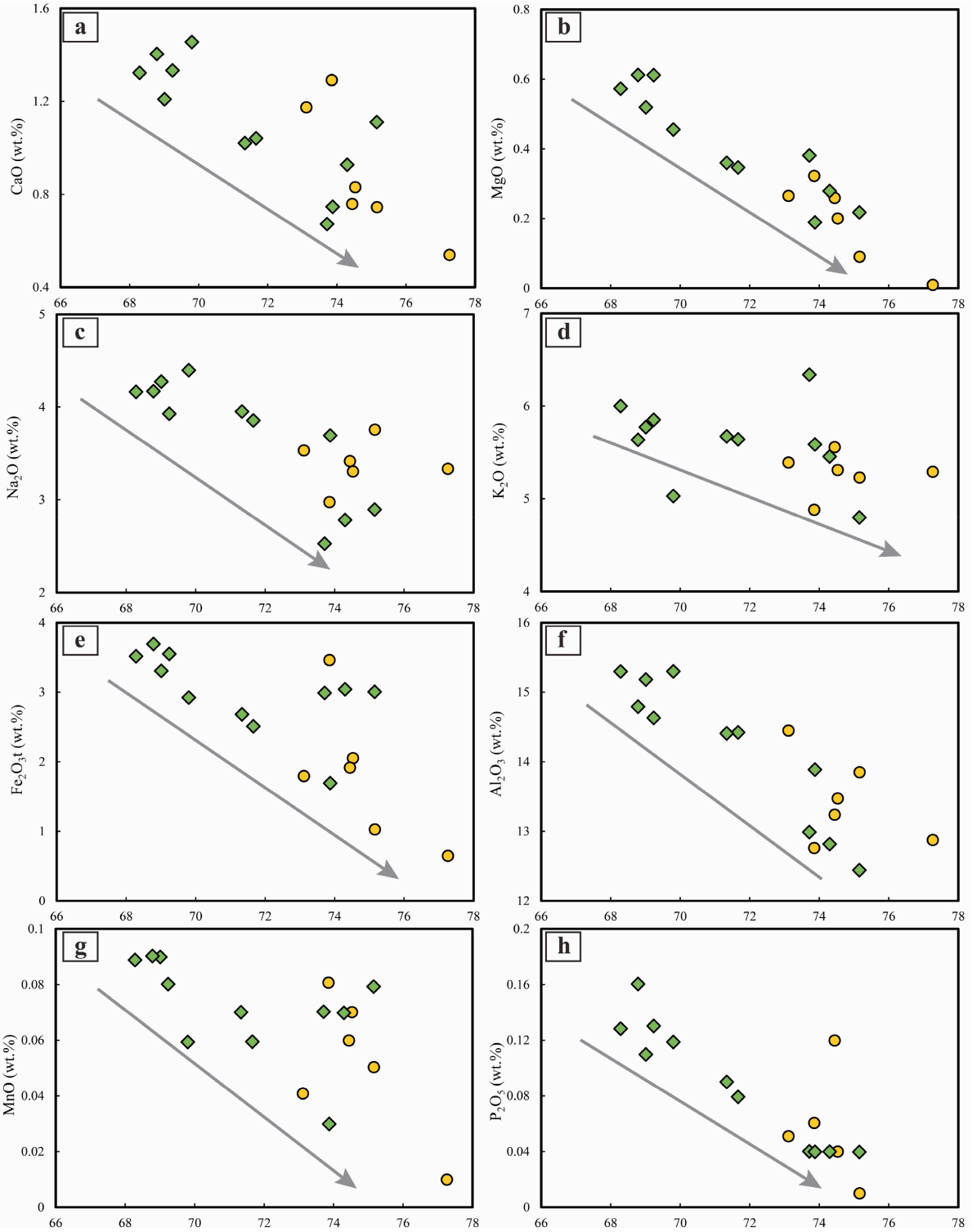
Figure 5. Discrimination diagrams showing the nomenclature and magmatic affinities of the granites in the study area. (a) R1 - R2 (cationic) diagram based on [53]; (b) $Na_2O + K_2O$ vs. SiO_2 diagram ([54] [58]); (c) K_2O vs. SiO_2 diagram ([54] [59]); (d) K_2O vs. Na_2O diagram ([55]); (e) Diagram of $(Al_2O_3 + CaO)/(FeOt + Na_2O + K_2O)$ vs. $100(MgO + FeOt + TiO_2)/SiO_2$ for $SiO_2 \geq 68\%$ [60]; Diagrams of $(Na_2O + K_2O - CaO)$ vs. SiO_2; (f) $FeOt/(FeOt + MgO)$ vs. SiO_2; (g) based on [56]; (h) A/NK vs. A/CNK diagram (in molar %) by [61].

[61]), the analyzed granites fall within the hyperaluminous region (A/CNK = 1.02 - 1.06; biotite granite) or straddle the metaluminous and hyperaluminous regions (A/CNK = 0.95 - 1.06; biotite and amphibole granite). Accordingly, normative corundum is observed in most of the analyzed granite samples, with the exception of four samples (MB58, MB08, MB56, and MB10) of biotite- and amphibole-bearing granite, which instead exhibit normative diopside (**Table 1**). The analyzed samples show a relatively homogeneous distribution and a negative linear trend among CaO, MgO, Na_2O, K_2O, Fe_2O_3t, Al_2O_3, MnO, P_2O_5, TiO_2, and SiO_2 (**Figures 6(a)-(i)**). Furthermore, their K_2O/Na_2O ratios (1.14 - 2.51) are greater than 1, which classifies them as potassic (**Figure 6(j)**).

4.2.2. Geochemistry of Trace Elements and Rare Earth Elements

The granites of the Djember Massif exhibit varied and high concentrations of Ba (314 - 1225 ppm), Zr (35 - 716 ppm), Sr (79.8 - 214 ppm), Rb (121 - 273 ppm), and Cr (83 - 195 ppm); but low concentrations of Y (2 - 119.5 ppm), Nb (1.32 - 41.2 ppm), Pb (24 - 46 ppm), Ni (1 - 3 ppm), and Co (1 - 3 ppm) (**Table 2**). As shown in **Figure 7**, the concentrations of Sr, Nb, and Zr are inversely correlated with SiO_2; whereas Cr abundances increase with increasing SiO_2 (**Figure 7(b)**, **Figure 7(d)**, **Figure 7(e)**, **Figure**

7(g)). The distribution of Ba, Rb, Pb, Th, and Y concentrations shows relative dispersion as a function of SiO_2 (Figure 7(a), Figure 7(c), Figure 7(f), Figure 7(h), Figure 7(i)). Furthermore, the Zr/Hf ratios decrease from biotite- and amphibole-bearing granite (32.06 - 46.09) to biotite-bearing granite (24.52 - 36.31), indicating an increasing fractionation index in these granites of the Djember Massif (Figure 7(j); [63]).



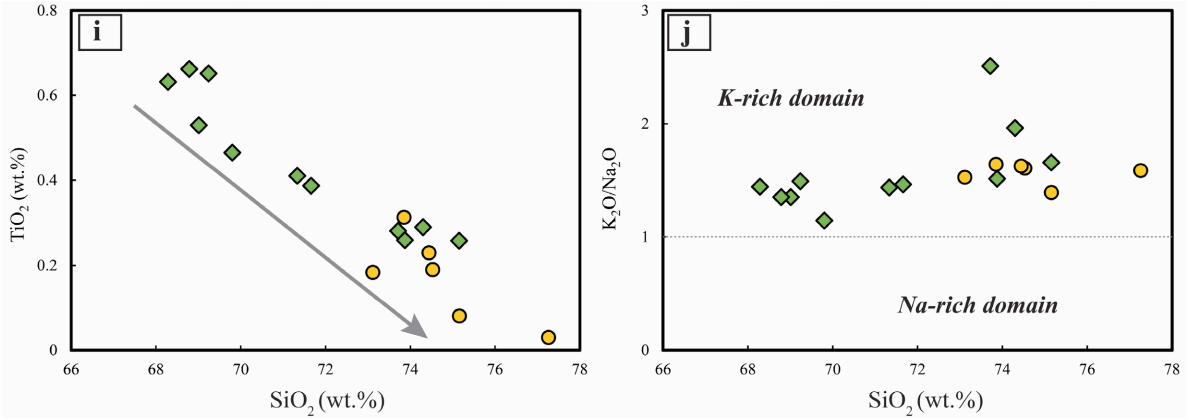


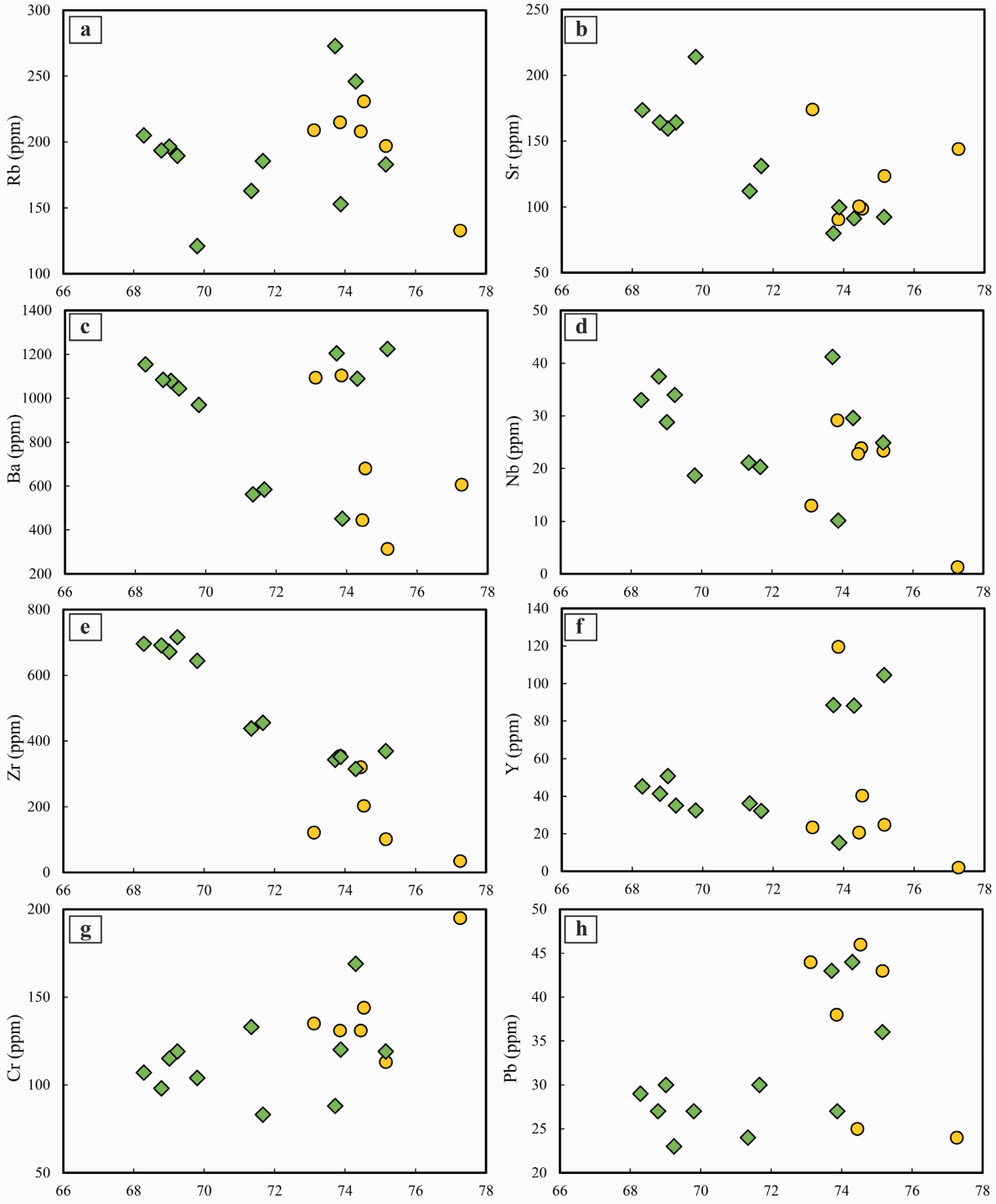
Figure 6. (a, b, c, d, e, f, g, h, i) [62] diagrams showing the variation of major elements as a function of silica in the analyzed granites; (j) K_2O/Na_2O vs. SiO_2 diagram showing the potassic nature of the granites in the study area.

The multi-element diagrams of the granites from the Djember Massif, normalized to the average values of the primitive mantle [64], reveal a strong enrichment in the most incompatible elements (e.g., Cs, Rb, Th, K, Pb...) compared to the less incompatible ones (Sr, P, Zr, Ti, etc.), with negative anomalies in Ba, Nb, Ta, Sr, P, Sm, and Ti, and positive anomalies in Th, K, Pb, Nd, and Zr (**Figure 8(a)**, **Figure 8(b)**). More specifically, the biotite granite shows certain profiles (samples MB05 and MB46) that are more depleted in P, Ti, and heavy rare earth elements (HREE) compared to the primitive mantle (**Figure 8(a)**). In the biotite and amphibole granite, the majority of samples exhibit a positive anomaly in Rb, with sample MB08 showing a more pronounced positive anomaly in Th and La (**Figure 8(b)**). All these geochemical characteristics are considered typical of crustal or magmatic arc rocks [65] [66]. Furthermore, the depletions in Ba, Sr, P, and Ti suggest that fractional crystallization of plagioclase, apatite, and ferro-titanium oxides was significant during the formation of these rocks [67]. Furthermore, the pronounced negative anomaly in Nb-Ta and positive anomaly in Pb suggest that the parent magma was of crustal origin or underwent significant contamination by crustal materials [23].

The rare earth elements in the granites of the study area are normalized to the chondrite values [68]. The rare earth element abundances (ΣREE) in biotite granite (43.32 - 584.62 ppm) and biotite-amphibole granite (292.43 - 848.45 ppm) show an enrichment in light rare earth elements (LREE) relative to heavy rare earth elements (HREE) (**Table 3**). This enrichment, which is also reflected in concentrations of light rare earth elements (ΣLREE = 37.53 - 496.77 ppm; 280.45 - 816 ppm, respectively) that are significantly higher than those of heavy rare earth elements (ΣHREE = 1.18 - 87.85 ppm; 11.98 - 68.13 ppm, respectively), is also illustrated in these rocks by negatively sloped profiles (**Figure 8(c)**, **Figure 8(d)**).

The profiles of the analyzed granites are generally homogeneous (**Figure 8(c)**, **Figure 8(d)**) and characterized by significant fractionation (i) [(La/Lu) N = 1.83 - 66.48] of LREE [(La/Sm)N = 1.32 - 21.19] relative to HREE [(Gd/Lu)N = 1.13 - 3.33] in the biotite granite (**Figure 8(c)**), and (ii) significant [(La/Lu)N = 5.82

- 44.06] fractionation of LREE [(La/Sm)N = 2.73 - 10.24] compared to HREE [(Gd/Lu)N = 1.51 - 2.58] in the biotite- and amphibole-bearing granite (Figure 8(d)). The Eu anomalies are predominantly negative and of moderate amplitude in the biotite and amphibole granite (Figure 8(d)), with EuN/Eu* = 0.41 - 0.57. In contrast, in the biotite granite, most of theREE profiles reveal the presence of pronounced negative Eu anomalies (EuN/Eu* = 0.36 - 0.50), with the exception



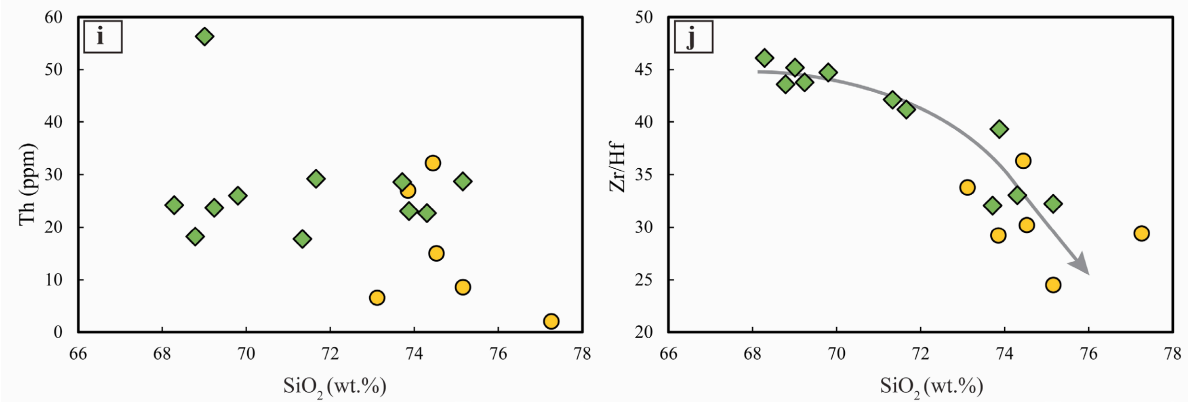


Figure 7. Variation of certain trace elements (a, b, c, d, e, f, g, h, i) and Zr/Hf ratios (j) as a function of silica content in the granites of the study area.

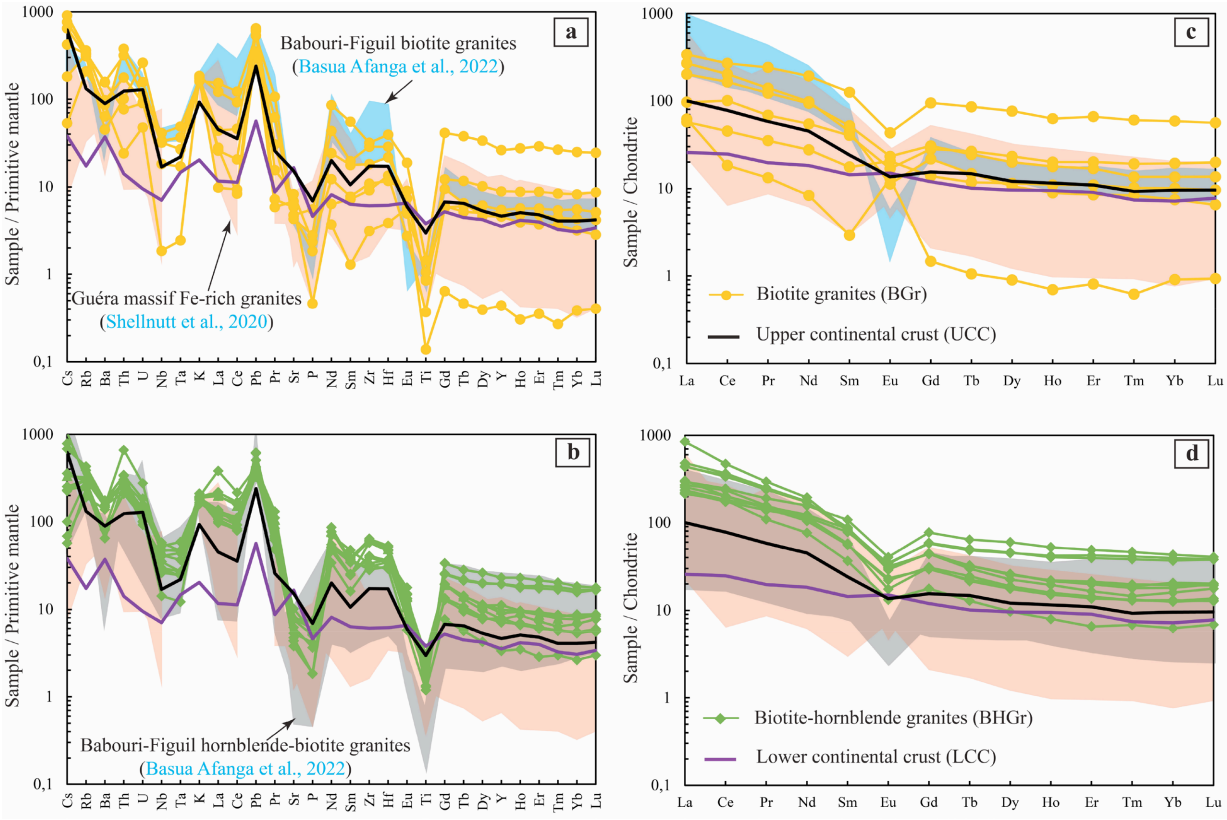


Figure 8. Multi-element diagrams normalized to the primitive mantle by [64] (a, b) and REE spectra normalized to chondrite [68] (c, d) for the granites of the study area. Data for the iron-bearing granites of the Guéra Massif ([34]) and the granites of the Babouri-Figuil magmatic complex [69] are plotted for comparison.

of two samples (MB05 and MB44), whose profiles are characterized by a positive Eu anomaly ranging from weak to strong (EuN/Eu* = 1.31 and 6.24) (**Figure 8(c)**). All of these negative Eu anomalies (EuN/Eu* = 0.36 - 0.57; **Table 3**) observed in the granites of the study area reflect significant fractionation of the plagioclases [70]. However, the positive Eu anomalies (EuN/Eu* = 1.31 and 6.24) observed in some samples of biotite granite could indicate the accumula-

tion of calcium plagioclase during the crystallization of the granitic magma or post-magmatic alteration processes.

5. Discussion

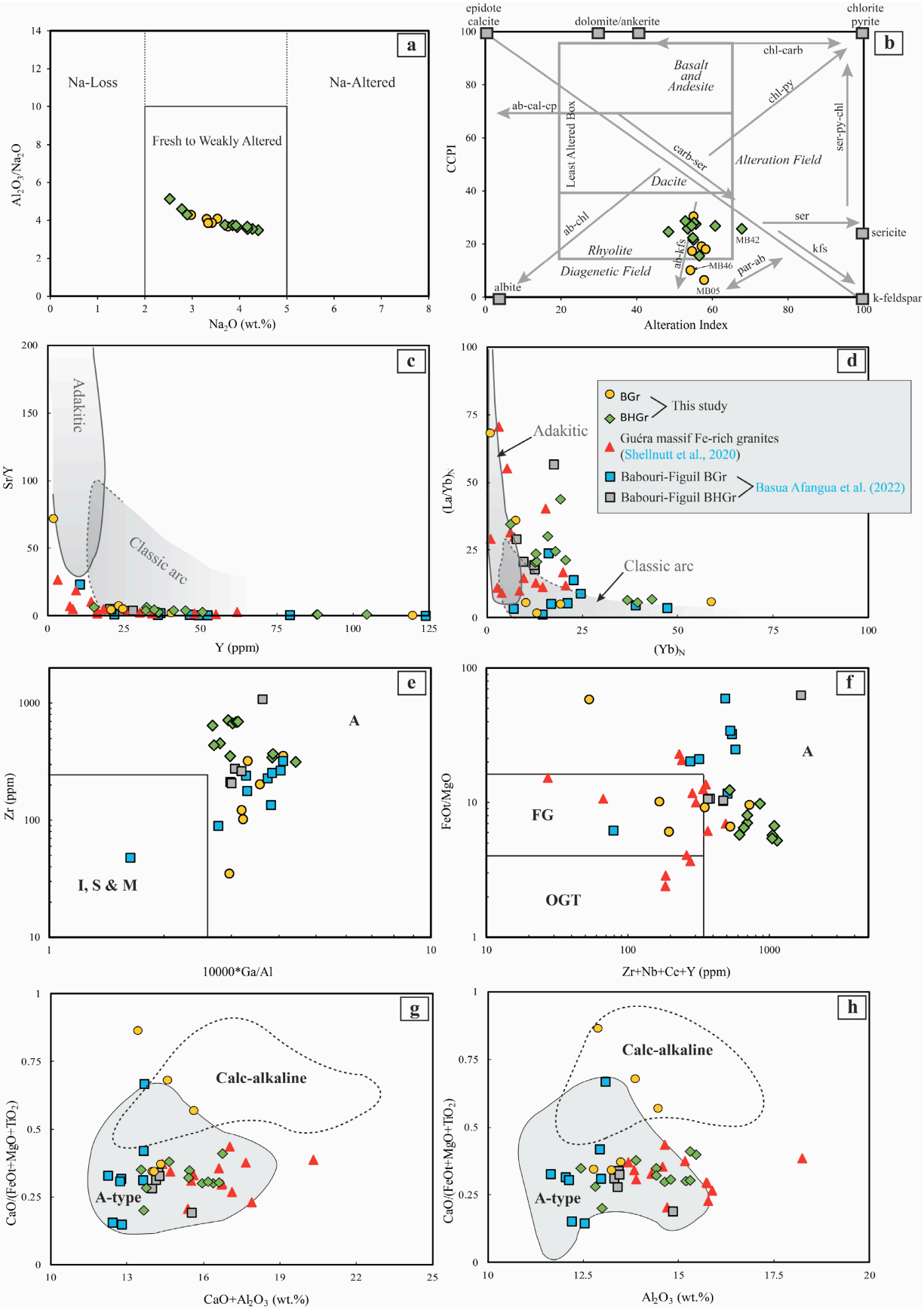
5.1. Alteration and Mobility of Chemical Elements

Since the major element, LILE, and HFSE compositions are used to constrain the magmatic history of the Djember Massif granites, it is therefore important to assess the impact of alteration on the geochemical characteristics of the analyzed samples. Although petrographic observations highlight the relative freshness of the collected samples, it should nevertheless be noted that zones of alteration consisting of sericite, damourite, and epidote were observed, which may indicate hydrothermal alteration. Indeed, studies based on the effect of weathering on the mobility of chemical elements and the geochemical characteristics of magmatic suites reveal that major oxides (e.g., Na_2O, K_2O, CaO) and LILE (e.g., Ba, Rb, Sr, Pb) are mobile, whereas HFSE (Ti, P, Hf, Zr, Nb, Ta, Y), transition metals (Co, Ni, V, Sc, Cr), and REEs (except Ce and Eu) are immobile and stable during weathering (e.g., [71] [72]).

To assess the degree of weathering in the analyzed granites, proxies such as LOI and the CeN/Ce* ratio are generally preferred. Indeed, samples with high LOI values (generally > 1%) and CeN/Ce* ratios greater than 1.1 and less than 0.9 are considered to be variably weathered [73]. The Djember granites exhibit low LOI values (0.29% - 0.73% in the BGr; 0.34% - 0.7% in the BHGr) and CeN/Ce* ratios ranging from 0.64 - 1.23 in the BGr and between 0.94 - 1.18 in the BHGr, indicating that they are generally slightly to moderately altered. Furthermore, these granites are plotted on the Al_2O_3/Na_2O vs. Na_2O alteration index diagram (**Figure 8(a)**; [74]). All BGr and BHGr samples are restricted to the range of unaltered to slightly altered rocks for which Na_2O is between 2% - 5% and Al_2O_3/Na_2O is < 10% (**Figure 8(a)**). This characteristic is supported by the alteration diagram by [75], which combines two distinct alteration indices (AI; [57]) reflecting the transformation of feldspar and the matrix into sericite and chlorite, relative to the chlorite-carbonate-pyrite index (CCPI; **Figure 9(b)**). Most of the granite samples fall within the low-alteration range for rhyolites (except MB46, MB05, and MB42) along the Ab-Kfs line (**Figure 9(b)**). However, given that their LOI values are <0.5%, these three samples are not excluded from the discussion. In light of the preceding discussion, it is therefore evident that the analyzed Djember granites are relatively unaltered and have preserved the geochemical signatures of their source materials, implying that the entire set of geochemical data can be used to constrain the nature, source, petrogenesis, and tectonic context of the granites of the Djember Massif.

5.2. Genetic Classification of the Granites of the Djember Massif

The granites of the Djember Massif are alkaline to calco-alkaline, iron-bearing, metalluminous to slightly hyperaluminous syenogranites, with A/CNK ratios generally < 1.1 and A/NK ratios generally > 1 (**Figure 5**). The observation of


a
Na-Loss
Na-Altered
Fresh to Weakly Altered
Al_2O_3/Na_2O
Na_2O (wt.%)
b
epidote calcite
dolomite/ankerite
chlorite pyrite
Basalt and Andesite
chl-carb
chl-py
ab-cal-cp
Least Altered Box
ser-py-chl
carb-ser
Alteration Field
Dacite
ab-chl
ser
sericite
MB42
Rhyolite
ab-kfs
kfs
MB46
par-ab
Diagenetic Field
albite
MB05
k-feldspar
CCPI
Alteration Index
c
Adakitic
Classic arc
Sr/Y
Y (ppm)
d
BGr
BHGr
This study
Guéra massif Fe-rich granites (Shellnutt et al., 2020)
Babouri-Figuil BGr
Babouri-Figuil BHGr
Basua Afangua et al. (2022)
Adakitic
Classic arc
$(La/Yb)_N$
$(Yb)_N$
e
A
I, S & M
Zr (ppm)
10000*Ga/Al
f
A
FG
OGT
FeOt/MgO
Zr+Nb+Ce+Y (ppm)
g
Calc-alkaline
A-type
$CaO/(FeOt+MgO+TiO_2)$
$CaO+Al_2O_3$ (wt.%)
h
Calc-alkaline
A-type
$CaO/(FeOt+MgO+TiO_2)$
Al_2O_3 (wt.%)

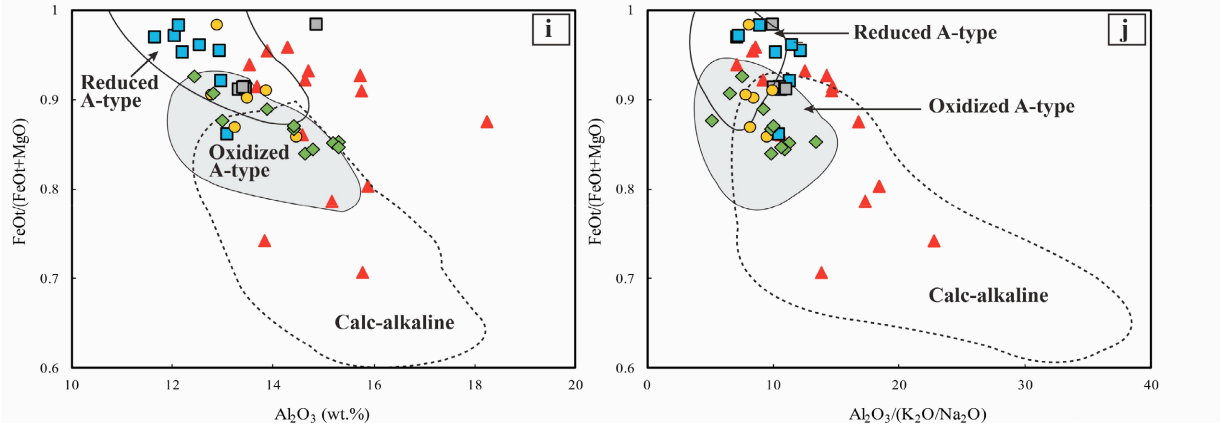


Figure 9. Geochemical classification diagrams for the granites of the study area. (a) Al_2O_3/Na_2O weathering index vs. Na_2O diagram [74]; (b) Weathering index diagram (AI; Ishikawa *et al.*, 1976 [57]) vs. CCPI by [75]; (c) and (d) Sr/Y vs. Y and (La/Yb)N vs. (Yb) N diagrams for distinguishing between typical adakitic and arc magmas (Defant and Drummond, 1990) [93]; (e, f) Zr vs. 10,000*Ga/Al and FeOt/MgO vs. Zr + Nb + Ce + Y diagrams [79]; (g, h, i, j) $CaO/(FeOt + MgO + TiO_2)$ vs. $CaO + Al_2O_3$, $CaO/(FeOt + MgO + TiO_2)$ vs. Al_2O_3, $FeOt/(FeOt + MgO)$ vs. Al_2O_3, $FeOt/(FeOt + MgO)$ vs. $Al_2O_3/(K_2O/Na_2O)$ [94]. Data for the iron-rich granites of the Guéra Massif [34] and the granites of the Babouri-Figuil magmatic complex [69] are plotted for comparison.

negative anomalies in Nb, Ta, P, and Ti, combined with a positive Pb anomaly, as well as high Th/Ta ratios (5.72 - 46.2) and Sr/Y < 100, with Y > 15 ppm, are diagnostic of arc materials typical of subduction zones (**Figure 9(c)**, **Figure 9(d)**, see **Figure 8(a)**, **Figure 8(b)**; [76] [77]). These characteristics are similar to those of granitic plutons surrounding the Djember Massif (e.g., Guéra, Lake Fitri, Ouaddaï, Mayo-Kebbi, Babouri-Figuil) in southern and western Chad, and the Cameroon-Chad border region (e.g., [34] [35] [48] [69] [78]). Furthermore, magmatic petrology has enabled the effective classification of granites into -M, -S, -I, and -A types based on the nature of their protolith (e.g., [79]-[81]). Type-M granites derive primarily from the crystallization of mantle magmas whose characteristics are inherent to the mantle (see [82]). However, given their high SiO_2 content (>67%) and low MgO content (<0.7%), the Djember granites are not Type-M granites. In contrast to Type-M granites, Type-S granites are primarily characterized by their high ASI values (>1.1) and the consistent presence of muscovite, garnet, and/or cordierite in their mineral composition [81] [83]; since the analyzed granites do not exhibit these aforementioned characteristics, they cannot belong to the S-type.

Distinguishing between Type-A and Type-I granites is not always easy, especially when dealing with highly fractionated Type-I granites. Petrographically, the mineral assemblage [brown biotite + allanite + titanite] is considered characteristic of Type-I granites (e.g., [84]). In contrast, the presence of alkaline mafic minerals such as aegirine, arfvedsonite, or riebeckite has historically been considered characteristic of Type-A granites [85]-[87]. Since petrographic observations have shown that the Djember granites lack these minerals, their geochemical composition is therefore the most objective criterion for distinguishing between Type I and Type A granites. Furthermore, the analyzed granites exhibit relatively high concentrations of SiO_2, K_2O, $Na_2O + K_2O$, Zr (especially > 250 ppm), Nb, Zr + Nb

+ Ce + Y (especially > 350 ppm, except for certain BGr), HFSE (e.g., Ga, Zr), as well as high FeO/(FeO + MgO), TiO_2/MgO, and Ga/Al, and low contents of CaO, MgO, P_2O_5, Ni, and Cr. Furthermore, they exhibit negative anomalies in Ba, Sr, P, Eu, and Ti, as well as high abundances of LILE (including Ba, Rb, and Th). All of these geochemical characteristics are considered typical of Type-A granites (e.g., [79] [88]-[90]), consistent with the diagram in **Figure 5(g)** [56].

In the Zr vs. 104Ga/Al and FeOt/MgO vs. Zr + Nb + Ce + Y discrimination diagrams (**Figure 9(e)**, **Figure 9(f)**; [79]), the BHGr samples are confined to the Type-A granite domain, similar to the granites of the Babouri-Figuil magmatic complex [69]. However, the analyzed BGr samples overlap the domains of highly fractionated Type I granite and Type A granite, similar to the iron-bearing granites of the Guéra Massif [34]. Although these analyzed BGr samples exhibit geochemical similarities to Type-A granites, their Zr (35 - 355 ppm) and Zr + Nb + Ce + Y (53.12 - 721.7 ppm) concentrations overlap the upper limit of the typical Type-A granite range (Zr = 250 ppm; Zr + Nb + Ce + Y = 350 ppm). These characteristics of the analyzed BGr suggest that it is formed from highly fractionated granitic magma [91] [92]. Indeed, [79] proposed that highly fractionated Type I felsic granites would exhibit values for certain trace and major elements, as well as Ga/Al ratios, that overlap with those of typical Type A granites. Thus, the Type-A signature of the BGr in the study area could be explained by significant fractional crystallization of the hyperaluminous Type-I magma. This hypothesis is further supported by [60] alkalinity index, which characterizes the analyzed BGr as a highly fractionated calc-alkaline granite (see **Figure 5(e)**).

Based on the classification system of [94], it is possible to distinguish calc-alkaline granites from Type-A granites, and oxidized Type-A granites from reduced Type-A granites. Accordingly, the granites of the Djember Massif are predominantly Type-A granites (with the exception of three samples from the BGr), as illustrated in **Figure 9(g)**, **Figure 9(h)**, similar to the iron-bearing granites of the Guéra Massif [34] as well as the granites of the Babouri-Figuil magmatic complex [69]. Furthermore, the BGr and BHGr in the study area belong to the group of oxidized Type-A granites, with the exception of the MB05 sample from the BGr, which falls within the reduced Type-A granite domain (**Figure 9(i)**, **Figure 9(j)**). This oxidized character of the analyzed granites differs from the iron-bearing granites of the Guéra Massif [34], as well as from the granites of the Babouri-Figuil magmatic complex [69], which generally show an affinity for reduced Type-A granites.

5.3. Magma Source and Petrogenesis of the Granites of the Djember Massif

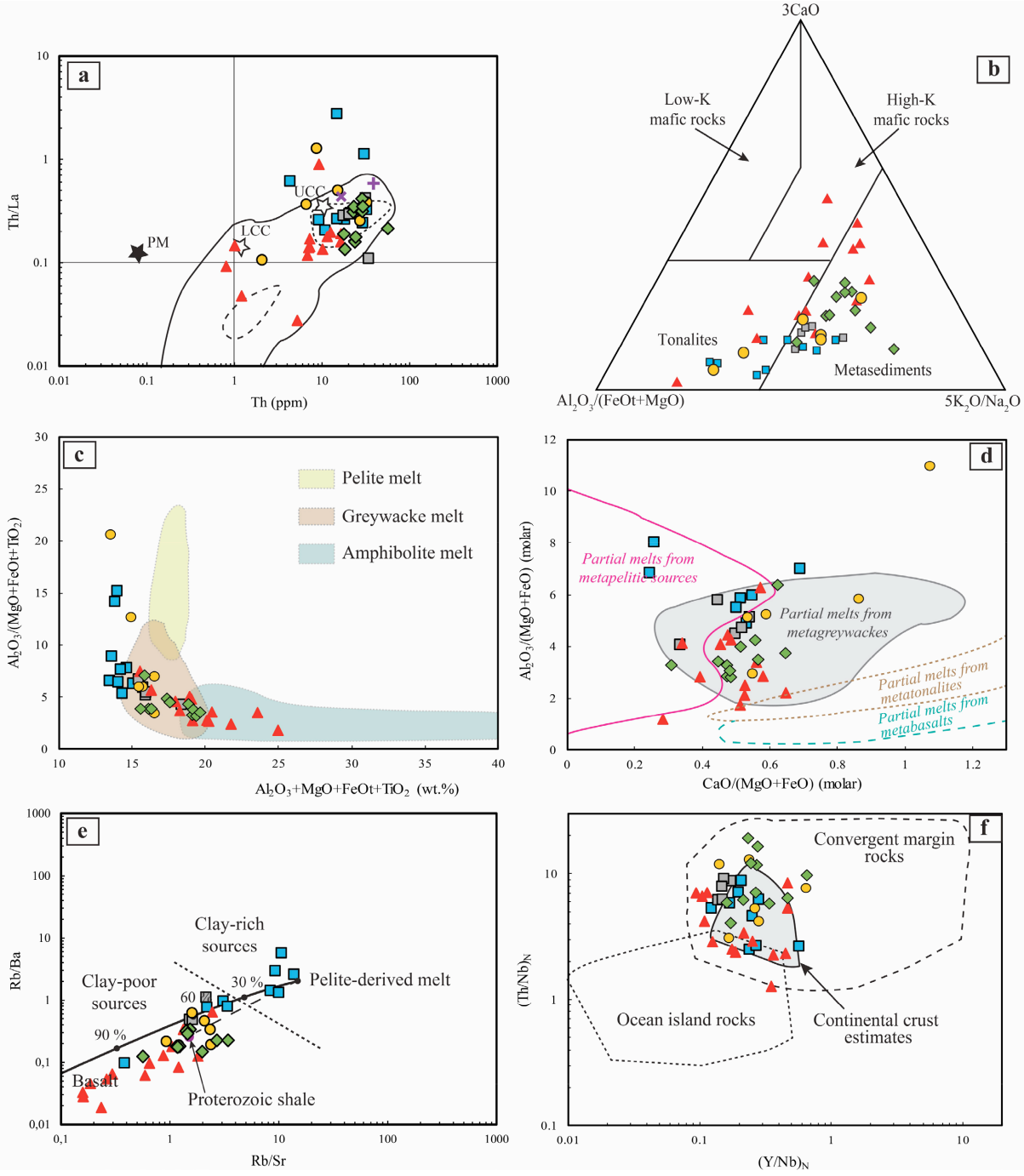
Although Type-A granites have historically been known to form through the crystallization of alkaline basaltic magma derived from the mantle with or without crustal contamination (e.g., [95] [96]), or through mixing between mantle magma and crustal materials (e.g., [97] [98]), recent studies in magmatic petrology have proposed new models of genesis, including: (i) partial melting of quartz-feldspar rocks (felsic granulites) within lower-to-middle crustal lithologies [90] [99], and

(ii) partial melting of quartz-feldspar igneous sources with contributions from metasedimentary rocks [95] [100].

Rb/Sr ratios are considered an important indicator of mantle-crust interaction. Mantle rocks have very low Rb/Sr ratios (0.01 - 0.1) compared to the lower (Rb/Sr = 0.12) and intermediate (Rb/Sr = 0.22) continental crust ([101] [102]) and even upper continental crust (Rb/Sr ≥ 0.5; [83]). The Rb/Sr ratios of the BGr (0.92 - 2.38) and BHGr (0.57 - 3.42) are far higher than those of mantle rocks, but fall within the range of ratios found in the upper continental crust. Furthermore, Nb/Ce ratios in the mantle are 0.39 [64] compared to 0.23 in the crust [103]. By comparison, these ratios range from 0.09 to 1.41 in the BGr and from 0.07 to 0.29 in the BHGr, bringing them closer to the values typical of the continental crust. The Sm/Nd ratios range from 0.11 to 0.37 in the BGr and from 0.14 to 0.22 in the BHGr, bringing them closer to the representative value for the continental crust (Sm/Nd = 0.2; [83]); this therefore suggests that the granitic magmas in the study area were derived primarily from the continental crust. This hypothesis is also supported by the low Mg# values (3.73 - 30.24) in the analyzed granites, which considerably reduce the likelihood of crust-mantle magmatic mixing; since crust-mantle magmatic mixing generally produces microdioritic inclusions and/or mineral disequilibrium patterns (which were not observed in the analyzed granites; see Section 4.1), thereby increasing the Mg# values of the residual liquids [104] [105]. Thus, such low Mg# values (<30) strongly support the melting of purely crustal sources to generate the granitic magmas that crystallized the BGr and BHGr of the Djember Massif.

The Th/La ratios (0.11 - 1.28 in the BGr; 0.13 - 0.42 in the BHGr) suggest that the source of the Djember Massif granites is likely supracrustal sediments, similar to the sources of the Babouri-Figuil granites [69] and the iron-bearing granites of Guéra [34]; and these ratios are comparable to the average Th/La ratios of intermediate to felsic rocks (**Figure 10(a)**; [106]). Furthermore, the composition of the source rocks for the analyzed granites can also be estimated using the Al_2O_3/TiO_2 ratio. Generally, this ratio ranges from 3 to 8 for mafic rocks, from 8 to 21 for intermediate igneous rocks, and from 21 to 70 for felsic igneous rocks [107]. In the granites of the Djember Massif, this Al_2O_3/TiO_2 ratio ranges from 40.81 to 430 in the BGr and from 22.35 to 53.65 in the BHGr, suggesting that the source of the analyzed granites included sediments derived from felsic igneous rocks. Accordingly, in the $Al_2O_3/(FeO + MgO)$-$3CaO$-$5K_2O/Na_2O$ triangular diagram by [108], the analyzed granites mostly show similarities to magmas resulting from the partial melting of metasediments that are thought to derive primarily from supracrustal rocks (**Figure 10(b)**), with the exception of two BGr and one BHGr samples, which instead indicate a tonalitic crustal source; such geochemical characteristics are also shared by both the Babouri-Figuil granites [69] and the iron-bearing granites of Guéra [34]. Furthermore, the source metasediments of these analyzed granites are believed to be (meta)grauwackes, as illustrated in **Figure 10(c)**, **Figure 10(d)** [109] [110], comparable to the source rocks of the Guéra and Babouri-Figuil granites [34] [69]. Furthermore, the enrichment of feldspars and biotite in Rb, Ba, and Sr affects the Rb/Ba and Rb/Sr ratios, which may reflect the composition of the source of the aluminosilicate

magma. Indeed, the Rb/Ba and Rb/Sr ratios are low in the analyzed granites and similar to those in the iron-bearing granites of Guéra [34], the BHGr and certain BGr from Babouri-Figuil [69], indicating a significant proportion of plagioclase in the source of the Djember Massif granites (**Figure 10(e)**; [111]). Consequently, the source of the granites in the study area is thought to have consisted of immature grauwackes and quartz-feldspar igneous materials. The Th/Nb vs. Y/Nb ratio (**Figure 10(f)**) shows that the samples from the study area fall almost entirely within the range typical of rocks from convergent margins.



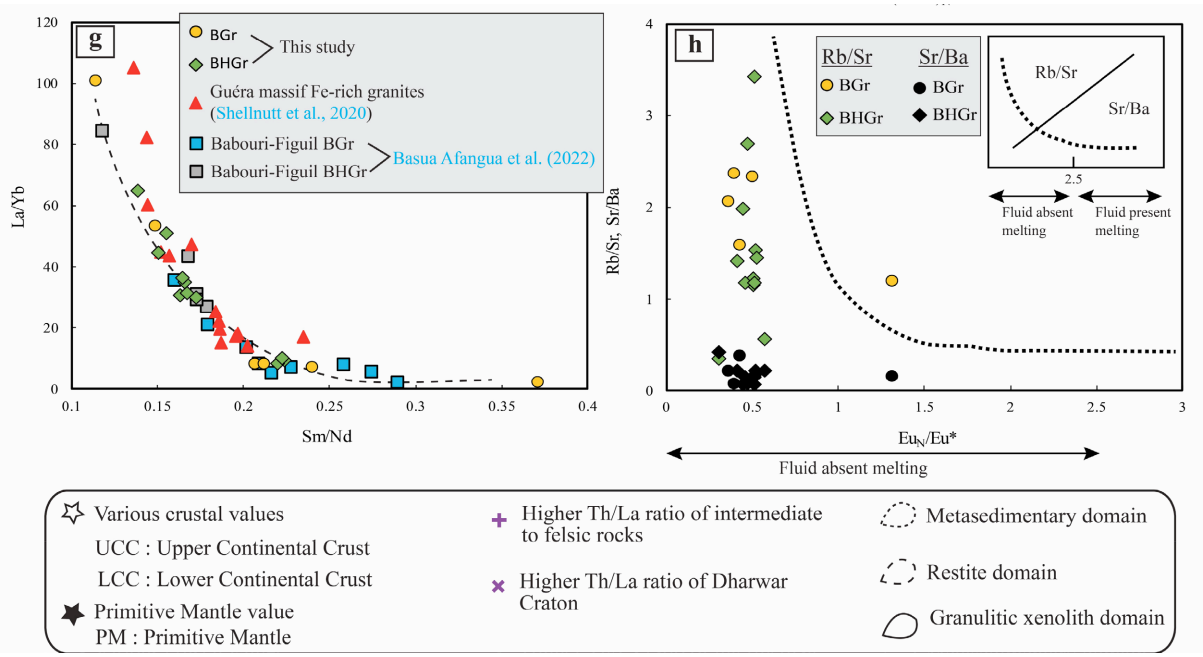


Figure 10. Discrimination diagrams showing the source and origin of the granites in the study area. (a) Th/La vs. Th diagram [106]; (b) ternary Al_2O_3/(FeOt + MgO)-3CaO-5K_2O/Na_2O diagram (Laurent *et al.*, 2014) [108]; (c) Al_2O_3/(MgO + FeOt + TiO_2) vs. Al_2O_3 + FeOt + MgO + TiO_2 diagram [109] [110]; (d) molar Al_2O_3/(MgO + FeOt) vs. molar CaO/(MgO + FeOt) diagram [109]; (e) Rb/Sr vs. Rb/Ba diagram [111] [114]; (f) (Y/Nb)N vs. (Th/Nb)N diagram [115]; (g) La/Yb vs. Sm/Nd diagram [116]; (h) Rb/Sr and Sr/Ba vs. EuN/Eu* diagram [117] [118]). Data from the iron-bearing granites of the Guéra Massif [34] and the granites of the Babouri-Figuil magmatic complex [69] are plotted for comparison.

The analyzed granites exhibit relatively high Zr contents (35 - 716 ppm), suggesting that the source materials were likely zircon-rich [84]. Furthermore, the relatively high K_2O contents (4.80% - 6.34%) in the analyzed granites imply the presence of potassium-rich minerals such as phlogopite (biotite), potassium amphibole, or potassium feldspar in their source rock. Indeed, [112] suggested that granitic magmas in equilibrium with phlogopite have high Rb/Sr ratios (>0.1) and low Ba/Rb ratios (<15) compared to granitic magmas in equilibrium with amphibole (Rb/Sr < 0.06 and Ba/Rb > 15). The Rb/Sr ratios of the granites from the Djember Massif are well above 0.1 and range from 0.57 to 3.42; their Ba/Rb values (1.59 to 8.02) are well below 15. These ratios suggest that phlogopite (biotite), rather than amphibole, was present, in association with feldspars, in the source rocks of the BGr and BHGr in the study area [87] [112]. Thus, the distinct chemistry exhibited by the analyzed granites would therefore be attributed to the heterogeneity of their source rather than to a mixture of mantle and crustal magma. Source heterogeneity can indeed be transferred to granitic magmas through the genesis of discrete magma batches [113].

Furthermore, the genesis of granitic magmas is not solely controlled by the nature of the source, but primarily by the conditions of crustal anatexis [119]. The observation of LREE and Zr enrichment, associated with negative Eu anomalies in the profiles of the analyzed granites (**Figure 8**), would indicate a low rate of partial melting without effective separation of their source rocks [120]-[122]. Since Nd is more

incompatible than Sm, the analyzed granites therefore exhibit low Sm/Nd ratios (0.11 - 0.37; mostly < 0.23) consistent with a low degree of partial melting. A low degree of partial melting in the source rock of the Djember Massif granites, similar to the results of regional studies [34] [69], is also supported by the negative correlation between La/Yb and Sm/Nd (**Figure 10(g)**; [116]). Furthermore, [117] established that low Rb/Sr ratios (<5) in aluminosilicate granites indicate the contribution of biotite, whereas high Rb/Sr ratios (>5) suggest the contribution of muscovite during magma generation. The analyzed granites have Rb/Sr ratios ranging from 0.57 to 3.42 (mostly < 5). Consequently, the genesis of the magmas of these granites likely involved the decomposition of biotite during partial melting. This is confirmed in the Ba vs. Pb diagram (**Figure 11(c)**), which shows that dehydrated/limited melting of biotite was the dominant mechanism in the formation of the magmas of the granites in the study area (e.g., [118]). The high Rb/Sr and Ba/Sr ratios (2.54 - 15.10, mostly > 4) in these granites support this mechanism of magma formation; however, their very low Sr/Ba ratios (0.07 - 0.39), combined with negative Eu anomalies, indicate that the granites in the study area likely originated from the partial melting of metasedimentary protolites under various conditions of low hydration (**Figure 10(h)**). This hypothesis is further supported by the relative abundance of hydrated minerals (biotite, amphibole) in these granites of the Djember Massif. The abundance of granitic massifs in the region is consistent with widespread crustal anatexis (e.g., [34] [69] [123]).

An additional constraint on the source of the analyzed granites comes from the Y/Nb ratios, which remain relatively constant during the fractionation of type-A magmas [88] [98]. Low Y/Nb ratios (<1.2) characterize mantle sources, whereas high Y/Nb ratios (>1.2) are diagnostic of continental sources, reflecting the high ratio in the continental crust [88]. The BGr exhibits high Y/Nb ratios (0.91 - 4.09, mostly > 1.2) comparable to the Y/Nb ratios in the BHGr (1.03 - 4.20, mostly > 1.2), indicating that the magmas formed through partial melting of crustal materials. A consistent result is obtained in the (Th/Nb)N vs. (Y/Nb)N diagram by [115], which shows that the analyzed granite samples fall within the compositional range of estimates for the continental crust in a convergent margin setting, similar to the granites of Guéra and Babouri-Figuil [34] [69]. These relationships suggest the melting of continental crustal components in the genesis of the granites in the study area within a convergent margin setting that is, in a collisional tectonic context which is also corroborated by negative anomalies in Nb, Sr, and Ti, and positive anomalies in Pb, Th, and K in the multi-element diagrams (**Figure 8(a)**, **Figure 8(b)**).

5.4. Evolutionary Processes and Crystallization Conditions of Magmas

Although the source is considered the primary control on the chemistry of granitic magmas [124], the geochemical composition of granites can also be determined by subsequent magmatic processes such as magma mixing [125], fractional crystallization with assimilation of host rocks [126], as well as the fundamental control

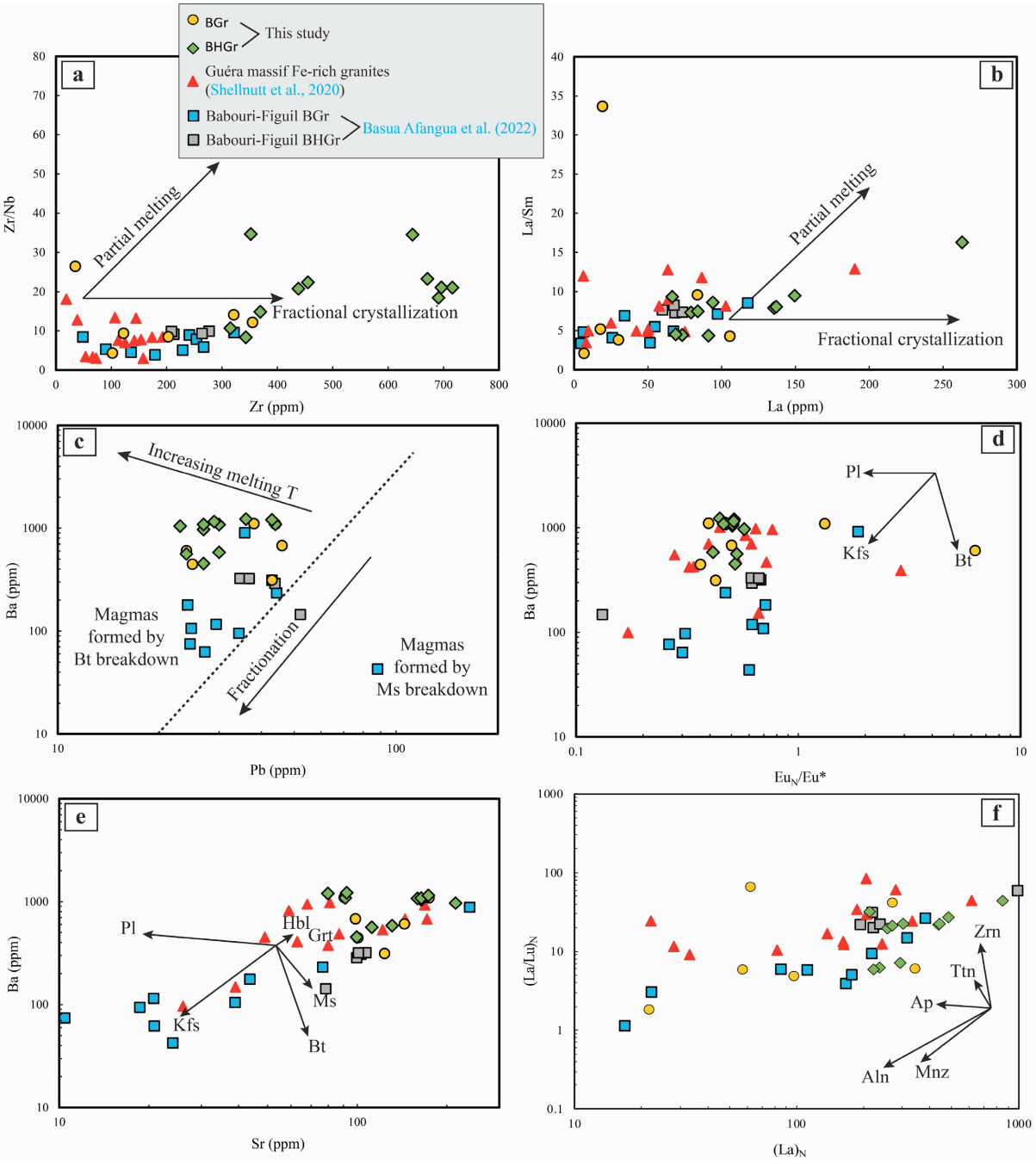
of partial melting [127] [128]. The granites in the study area exhibit negative-slope linear distributions, reflecting a drastic reduction in the concentration of major and trace elements as SiO_2 increases (see **Figure 6**, **Figure 7**), a characteristic that rules out magma mixing but instead suggests evolution through fractional crystallization of a less fractionated magma, consistent with the work of several researchers (e.g., [129] [130]). In fact, in the Zr/Nb vs. Zr and La/Sm vs. La diagrams (**Figure 11(a)**, **Figure 11(b)**), the analyzed granites align along a horizontal trajectory, suggesting that the chemical composition of the granitic magmas was likely controlled by a variable degree of fractional crystallization [131], similar to the observations made by [34] and [69] in the Guéra and Babouri-Figuil granites, respectively. This is further supported by the decrease in Zr/Hf ratios with increasing SiO_2 (**Figure 7(j)**), reflecting a process of normal magmatic differentiation via fractional crystallization. Furthermore, the Ba vs. EuN/Eu* and vs. Sr diagrams (**Figure 11(d)**, **Figure 11(e)**) show that alkali feldspar is the mineral that controls variations in Ba. Consistent with the work of [132], these observations suggest that the fractionation of alkali feldspar is the primary mineral phase in the magmatic evolution of the granites in the study area. Furthermore, a fractionation process involving accessory phases rich in REEs, such as apatite, titanite, allanite, and zircon is clearly reflected by negative (P, Ti, and Zr) and positive (La and Ce) anomalies in the spectra of the multi-element diagrams (**Figure 8(a)**, **Figure 8(b)**), since these accessory minerals are widely observed in the granites described in this study. Accordingly, in the (La/Lu) N vs. LaN diagram (**Figure 11(f)**), the variation in REE abundances is consistent with the fractionation of apatite and allanite. Titanite and zircon do not appear to have exerted a significant influence on the variation in REE concentrations in the granites of the study area. A similar petrogenetic evolution has been previously described for the Guéra and Babouri-Figuil granites [34] [69].

Furthermore, the crystallization conditions (temperature, pressure) of the granitic magma, estimated from the whole-rock geochemical composition by plotting the samples on Zr vs. (Na + K + 2Ca)/(Al * Si) diagrams (**Figure 11(g)**; [133] [134]) and Ab-An-Or diagrams (**Figure 11(h)**; [135]), range from (~650˚C to +850˚C and ~1 to ~3 kb) in the BGr and (+850˚C and 1 to 3 kb) in the BHGr. Such temperatures and pressures indicate a shallow depth of crustal emplacement—likely at the boundary between the upper and middle crust [136] for the BGr and BHGr samples analyzed, similar to the crystallization conditions of Type-A granites described in the literature (e.g., [48] [87] [115]) as well as the Babouri-Figuil granites (689˚C - 909˚C, 0.3 - 2 kb, and 0.8 - 5.5 km for the BGr; 842˚C - 1079˚C, 2.2 - 2.5 kb, and 6.2 - 6.7 km for BHGr; [69]).

5.5. Tectonic Context of Granitic Magma Formation

To determine the tectonic context of the granites described in this study, the tectonic discrimination diagrams for granitic rocks based on [137] are used. In the Ta vs. Yb diagram (**Figure 12(a)**), the granites studied are distributed between the

volcanic arc granite (VAG) domain and the field of intraplate granites and alumina-rich ridges of the MORB. However, the tectonic context of the granites studied overlaps the intersection of syn-collisional granites (syn-COLG), volcanic arc granites (VAG), and intraplate granites (WPG) (**Figure 12(b)**). Consequently, the granites described in this study remain controversial, and samples straddling this intersection zone would be considered to belong to the post-collisional granites (post-COLG) field (**Figure 12(b)**; [138]). Thus, the granites of the Djember Massif can be clearly classified as post-collisional granites [61] [138], similar to the Babouri-Figuil granites [69].



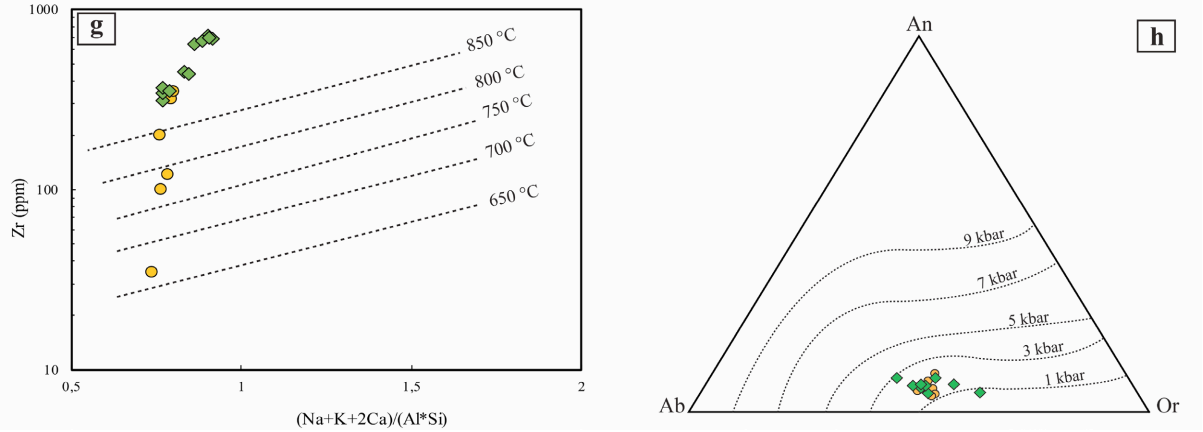


Figure 11. Discrimination diagrams showing the evolution of granitic magmas in the study area. (a) Zr/Nb vs. Zr diagram; (b) La/Sm vs. La diagram [131]; (c) Pb vs. Ba diagram; (d, e) EuN/Eu * vs. Ba and Sr diagrams ([132]); (f) (La/Lu)N vs. LaN diagram.

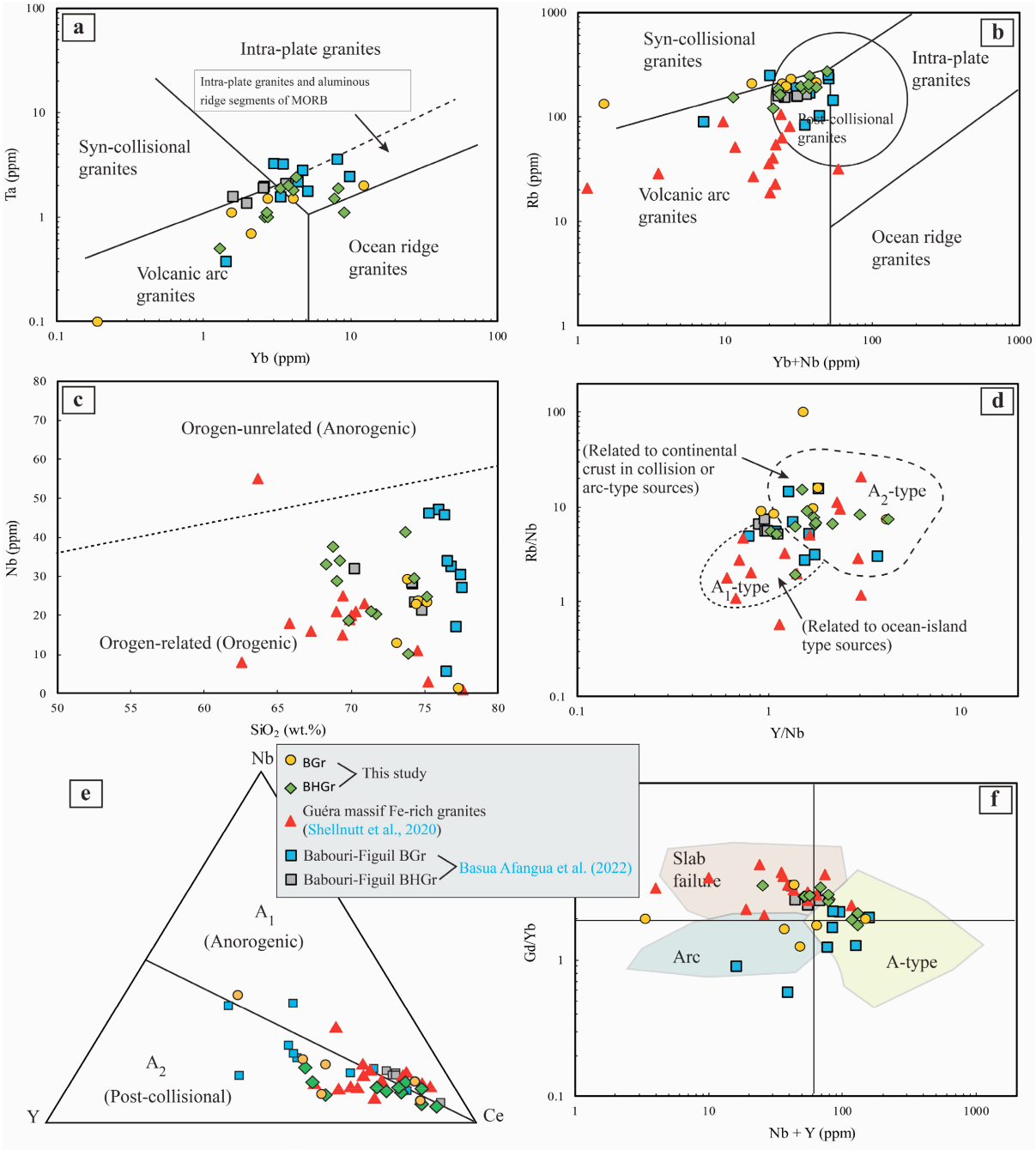
Although [95] historically defined Type-A granites as anorogenic granites, their exclusively anorogenic geotectonic context has been called into question; subsequent studies have suggested they formed in both anorogenic and orogenic contexts [79] [88]. The association of the granites in the study area with orogenesis specifically the Pan-African orogeny is evident in the Nb vs. SiO_2 diagram, in which all analyzed granites fall within the orogenic rock domain (**Figure 12(c)**), similar to the granites of Guéra and Baboui-Figuil [34] [69]. Furthermore, Type-A granites are subdivided into Type-A1 and Type-A2 based on tectonic contexts and sources [88]. This classification is based on Y/Nb ratios, with Type A1 (Y/Nb < 1.2) corresponding to anorogenic settings such as continental rifts or intraplate zones, and Type A2 (Y/Nb > 1.2) defining orogenic settings such as continental collisions or island arcs. The analyzed granites are characterized by Y/Nb ratios (0.91 - 4.2) that are predominantly > 1.2, indicating that most of them fall within the A2-type granite range, consistent with a post-collisional tectonic setting, as illustrated in the Rb/Nb vs. Y/Nb and Y-Ce-Nb diagrams (**Figure 10(d)**, **Figure 10(e)**). Similar geotectonic contexts have been described for plutonic intrusions on a regional scale (e.g., [34] [37] [41] [48] [69]).

Furthermore, field relationships, petrographic data, and geochemical signatures of the analyzed granites indicate that they are similar to intrusions from active continental margins (e.g., **Figure 12(g)**, **Figure 12(h)**). The samples show enrichment in LILLE (Rb, Th, U, and K) relative to HFSE (Nb, Ta, and Ti), reflecting a major continental margin setting with a significant contribution from the continental crust [88] (**Figure 8(a)**, **Figure 8(b)**). Furthermore, a continental arc setting is illustrated in the Ce/P_2O_5 vs. Zr/TiO_2 diagram by [140] for the granites of the study area (**Figure 12(g)**). This represents a normal continental arc setting, as indicated by the distribution of the analyzed granite samples in the Rb/Zr vs. Nb diagram by [67] (**Figure 12(h)**). Similar results are inferred for the Type-A granites of the Guéra and the Babouri-Figuil magmatic complex ([34] [69]). The continental arc-type signatures exhibited by the analyzed granites are therefore

thought to have been inherited from immature sediments (grauwackes) containing arc-derived detritus (e.g., [141] [142]).

5.6. Geodynamic Implications and Regional Correlation

The granites studied are located in the Djember region, north of Korbol (southern Chad) in the Guéra Massif. This massif is considered to lie along the southern boundary of the Saharan metacraton (e.g., [34] [123] [143]). The analyzed granites have sub-alkaline to alkaline, alumina-rich, and hyper-K to shoshonitic compositions, a characteristic common to granitoids formed in late- to post-tectonic



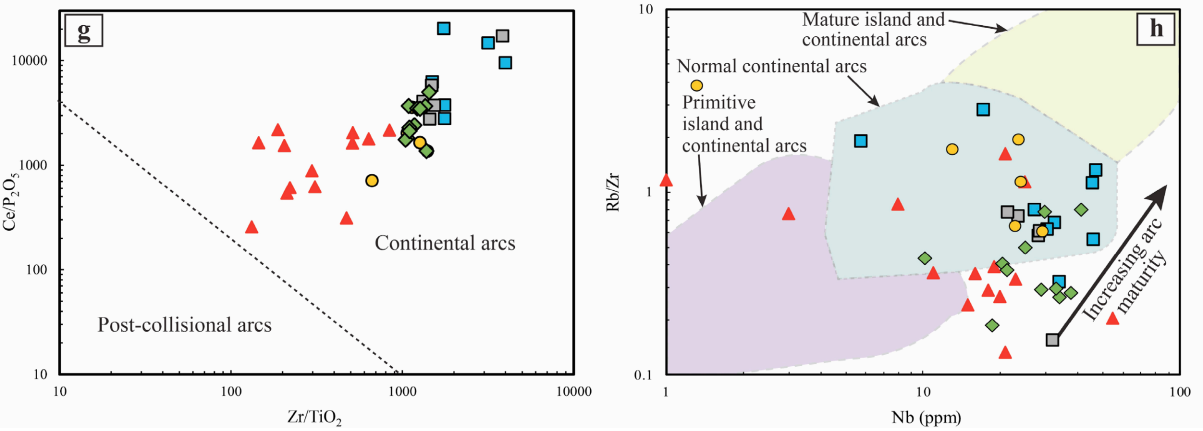


Figure 12. Determination of the geotectonic context of the granites in the study area. (a, b) Ta vs. Yb and Rb vs. Yb + Nb diagrams [137] [138]; (c) Nb vs. SiO_2 (%) diagram; (d) Rb/Nb vs. Y/Nb diagram [88]; (e) Y-Nb-Ce ternary diagram [88]; (f) Gd/Yb vs. Yb + Nb diagram (Whalen and Hildebrand, 2019) [139]; (g) Ce/P_2O_5 vs. Zr/TiO_2 diagram; (h) Nb vs. Rb/Zr diagram [67]). Data for the iron-bearing granites of the Guéra Massif [34] and the granites of the Babouri-Figuil magmatic complex [69] are plotted for comparison.

collisional settings [2] [144]. Indeed, the quartz ocelli observed in feldspar crystals suggest that these feldspars formed through textural growth in a relatively stable environment [122] [145]. Furthermore, these iron-rich granites are low in CaO, which makes them similar to the highly potassium-rich calc-alkaline granitoids (KCG) described by [23]. These geochemical characteristics, combined with the near absence of deformation structures, define post-tectonic granites formed in a post-collisional environment at the end of the collision between the West African/Congo cratons and the Saharan metacraton (e.g., [7] [14] [69] [123]). Positive anomalies in Rb, K, Th, U, and Pb indicate that the analyzed granites were emplaced in a lithospheric environment modified by subduction [69] [146]. In the Nb + Y vs. Gd/Yb diagram, the analyzed Type-A granites show an evolution from the plate break toward the Type-A granite field, but remain close to an arc (**Figure 12(f)**). This arc signature implies the presence of a subduction zone, which in this region is identified as the Chad Lineament. Indeed, [4] interpreted this tectonic structure as a possible oceanic suture zone, which extends into Cameroon via the Tcholliré-Banyo Fault interpreted as an ocean-continent subduction zone (e.g., [9] [147]-[149]). Furthermore, as with the Type-A granites of Guéra, Babouri-Figuil, and Mayo-Kébbi, such granitic rocks are most likely the result of crustal delamination (e.g., [1] [7] [78] [150]). In **Figure 12(f)**, they are consistent with crustal delamination induced by plate rupture [11] [69] [139]. Crustal delamination was proposed by [123] to explain the formation of the Late Ediacaran post-collisional Type-A granites of the Guéra Massif, which are dated to ~570 - 560 Ma [34] [36] [123] [151]. Thus, since our Type-A granites are post-collisional (**Figure 12**) and show little to no deformation, they would therefore indicate post-collisional magmatism, likely from the Late Ediacaran.

Several previous studies have shown that the transition from syn-collisional crustal thickening to post-collisional thinning in the Central African orogenic belt

(COAB) in Chad involved delamination of the thickened lithosphere and upwelling of the asthenosphere, leading to the melting of the continental crust and mantle and the massive production of post-collisional granitoids with type-A affinities (e.g., [34] [37] [48] [78] [123]). In the study area, this upwelling of mantle magma into the relaxing continental crust is thought to have provided the heat necessary for the partial melting of a heterogeneous, deeply buried source consisting of immature (meta) grauwackes and detritus of arc-derived quartz-feldspar igneous rocks. This model of mantle magma subduction inducing the partial melting of the heterogeneous crustal source of the analyzed granites is supported by the observation at outcrops of basic to intermediate rocks (amphibolites, gabbros, and quartz diorites) forming small massifs in the study area [152]. Among existing generic models, our model above is similar to the "low-pressure partial fusion of quartz-feldspar igneous sources with a contribution from metasedimentary rocks" model proposed by [94] and [100] for the genesis of type-A calc-alkaline, iron-bearing, and metalluminous to hyperaluminous granites. The absence of alkaline mafic minerals (e.g., aegirine, arfvedsonite, or riebeckite) in the BHGr suggests that their alkaline character may be due to enrichment by alkali-rich fluids derived from mantle magma ascending into the thinned continental crust, consistent with the high Ba/La (4.11 - 17.49) and K/Ti (11.79 - 31.25) ratios in the analyzed BHGr samples. The ascent of granitic magmas from their crustal source led to the emplacement of the BGr and BHGr in the upper continental crust of the southern Saharan metacraton (including the Korbol zone in southern Chad), a region known for its thinned lithosphere (~120 km thick; [7] [153]).

6. Conclusions

The main conclusions of this study are as follows:

- The Djember Massif, located in southern Chad, belongs to the COAC in the southern part of the Saharan metacraton. Biotite granite and biotite-amphibole (green hornblende) granite are exposed there. Their geochemical characteristics show that (i) the biotite granite is hyper-K calc-alkaline with a shoshonitic tendency, iron-bearing, and slightly hyperaluminous, as well as calc-alkaline to calc-alkaline with a strongly fractionated character; (ii) the biotite and amphibole granite is a hyper-K calc-alkaline granite with a shoshonitic tendency, iron-rich, and metaluminous to slightly hyperaluminous, with an alkaline to calc-alkaline affinity.
- The Djember granites correspond to oxidized Type A granites characterized by significant enrichments in LILE and LREE relative to HFSE and HREE, respectively. They are thought to have formed through low-pressure partial melting of heterogeneous crustal sources consisting of immature (meta)grauwackes associated with detritus of arc-derived quartz-feldspar igneous rocks, accompanied by fractional crystallization of the resulting granitic magmas.
- The Djember granites formed during the late- to post-tectonic phases of the Pan-African orogeny, associated with crustal delamination that followed lithospheric

thinning during the post-collisional evolution of the Pan-African system.

Acknowledgements

We would like to express our gratitude to the editor and anonymous reviewers for their critical comments on the manuscript.

Authors' Contributions

Mahamat Boka Ramadane: Conceptualization, Methodology, Software, Writing—original version. **Doumnang Mbaïgane Jean-Claude:** Conceptualization, Methodology, Software, Writing—original version. **Madjimbe Guiguindibaye:** Conceptualization, Methodology, Software, Copywriting—original version.

Conflicts of Interest

The authors declare no conflicts of interest regarding the publication of this paper.

References

[1] Abdelsalam, M.G., Gao, S.S. and Liégeois, J. (2011) Upper Mantle Structure of the Saharan Metacraton. *Journal of African Earth Sciences*, **60**, 328-336. https://doi.org/10.1016/j.jafrearsci.2011.03.009

[2] Black, R. and Liegeois, J. (1993) Cratons, Mobile Belts, Alkaline Rocks and Continental Lithospheric Mantle: The Pan-African Testimony. *Journal of the Geological Society*, **150**, 89-98. https://doi.org/10.1144/gsjgs.150.1.0088

[3] Ennih, N. and Liégeois, J. (2008) The Boundaries of the West African Craton, with Special Reference to the Basement of the Moroccan Metacratonic Anti-Atlas Belt. *Geological Society, London, Special Publications*, **297**, 1-17. https://doi.org/10.1144/sp297.1

[4] Garfunkel, Z. (2015) The Relations between Gondwana and the Adjacent Peripheral Cadomian Domain—Constrains on the Origin, History, and Paleogeography of the Peripheral Domain. *Gondwana Research*, **28**, 1257-1281. https://doi.org/10.1016/j.gr.2015.05.011

[5] Kennedy, W. (1964) The Structural Differentiation of Africa in the Pan-African (500 ± M. Y.) Tectonic Episode. 8th Annual Report of the Research Institute of African Geology, University of Leeds.

[6] Kröner, A. (1980) Pan African Crustal Evolution. *Episodes*, **3**, 3-8. https://doi.org/10.18814/epiiugs/1980/v3i2/001

[7] Liégeois, J., Abdelsalam, M.G., Ennih, N. and Ouabadi, A. (2013) Metacraton: Nature, Genesis and Behavior. *Gondwana Research*, **23**, 220-237. https://doi.org/10.1016/j.gr.2012.02.016

[8] Stern, R.J. (1994) Arc Assembly and Continental Collision in the Neoproterozoic East African Orogen: Implications for the Consolidation of Gondwanaland. *Annual Review of Earth and Planetary Sciences*, **22**, 319-351. https://doi.org/10.1146/annurev.ea.22.050194.001535

[9] Bouyo, M.H., Zhao, Y., Penaye, J., Zhang, S.H. and Njel, U.O. (2015) Neoproterozoic Subduction-Related Metavolcanic and Metasedimentary Rocks from the Rey Bouba Greenstone Belt of North-Central Cameroon in the Central African Fold Belt: New Insights into a Continental Arc Geodynamic Setting. *Precambrian Research*, **261**, 40-

53. https://doi.org/10.1016/j.precamres.2015.01.012

[10] Caby, R. (2003) Terrane Assembly and Geodynamic Evolution of Central-Western Hoggar: A Synthesis. *Journal of African Earth Sciences*, **37**, 133-159. https://doi.org/10.1016/j.jafrearsci.2003.05.003

[11] Liégeois, J.P., Latouche, L., Boughrara, M., Navez, J. and Guiraud, M. (2003) The LATEA Metacraton (Central Hoggar, Tuareg Shield, Algeria): Behaviour of an Old Passive Margin during the Pan-African Orogeny. *Journal of African Earth Sciences*, **37**, 161-190. https://doi.org/10.1016/j.jafrearsci.2003.05.004

[12] Triantafyllou, A., Berger, J., Baele, J., Diot, H., Ennih, N., Plissart, G., *et al.* (2016) The Tachakoucht-Iriri-Tourtit Arc Complex (Moroccan Anti-Atlas): Neoproterozoic Records of Polyphased Subduction-Accretion Dynamics during the Pan-African Orogeny. *Journal of Geodynamics*, **96**, 81-103. https://doi.org/10.1016/j.jog.2015.07.004

[13] Errami, E., Bonin, B., Laduron, D. and Lasri, L. (2009) Petrology and Geodynamic Significance of the Post-Collisional Pan-African Magmatism in the Eastern Saghro Area (Anti-Atlas, Morocco). *Journal of African Earth Sciences*, **55**, 105-124. https://doi.org/10.1016/j.jafrearsci.2009.02.006

[14] Liégeois, J., Navez, J., Hertogen, J. and Black, R. (1998) Contrasting Origin of Post-Collisional High-K Calc-Alkaline and Shoshonitic versus Alkaline and Peralkaline Granitoids. The Use of Sliding Normalization. *Lithos*, **45**, 1-28. https://doi.org/10.1016/s0024-4937(98)00023-1

[15] Toteu, S.F., Van Schmus, W.R., Penaye, J. and Michard, A. (2001) New U-Pb and Sm-Nd Data from North-Central Cameroon and Its Bearing on the Pre-Pan African History of Central Africa. *Precambrian Research*, **108**, 45-73. https://doi.org/10.1016/s0301-9268(00)00149-2

[16] Stern, R.J. (2002) Crustal Evolution in the East African Orogen: A Neodymium Isotopic Perspective. *Journal of African Earth Sciences*, **34**, 109-117. https://doi.org/10.1016/s0899-5362(02)00012-x

[17] Ngako, V., Affaton, P., Nnange, J.M. and Njanko, T. (2003) Pan-African Tectonic Evolution in Central and Southern Cameroon: Transpression and Transtension during Sinistral Shear Movements. *Journal of African Earth Sciences*, **36**, 207-214. https://doi.org/10.1016/s0899-5362(03)00023-x

[18] Njonfang, E., Ngako, V., Moreau, C., Affaton, P. and Diot, H. (2008) Restraining Bends in High Temperature Shear Zones: The "Central Cameroon Shear Zone", Central Africa. *Journal of African Earth Sciences*, **52**, 9-20. https://doi.org/10.1016/j.jafrearsci.2008.03.002

[19] Toteu, S.F., Penaye, J. and Djomani, Y.P. (2004) Geodynamic Evolution of the Pan-African Belt in Central Africa with Special Reference to Cameroon. *Canadian Journal of Earth Sciences*, **41**, 73-85. https://doi.org/10.1139/e03-079

[20] Pin, C. and Poidevin, J. (1987) U-Pb Zircon Evidence for a Pan-African Granulite Facies Metamorphism in the Central African Republic. A New Interpretation of the High-Grade Series of the Northern Border of the Congo Craton. *Precambrian Research*, **36**, 303-312. https://doi.org/10.1016/0301-9268(87)90027-1

[21] Clarke, D.B. (1981) The Mineralogy of Peraluminous Granites: A Review. *The Canadian Mineralogist*, **19**, 3-17.

[22] Hutton, D.H.W. (1988) Granite Emplacement Mechanisms and Tectonic Controls: Inferences from Deformation Studies. *Earth and Environmental Science Transactions of the Royal Society of Edinburgh*, **79**, 245-255. https://doi.org/10.1017/s0263593300014255

[23] Barbarin, B. (1999) A Review of the Relationships between Granitoid Types, Their Origins and Their Geodynamic Environments. *Lithos*, **46**, 605-626. https://doi.org/10.1016/s0024-4937(98)00085-1

[24] Bessoles, B. and Trompette, M. (1980) Géologie de l'Afrique: La chaîne panafri-caine, "Zone mobile d'Afrique Central (partie sud) et zone mobile soudanaise". *Mémoire du Bureau de Recherche Géologiques et Minières*, No. 92, Article 396.

[25] Doumnang, J.C. (2006) La géologie des formations néoprotérozoïques du mayo-kebbi (SW du Tchad). Thèse de Doctorat, Université d'Orléans, 206 p.

[26] Penaye, J., Kröner, A., Toteu, S.F., Van Schmus, W.R. and Doumnang, J. (2006) Evolution of the Mayo Kebbi Region as Revealed by Zircon Dating: An Early (Ca. 740Ma) Pan-African Magmatic Arc in Southwestern Chad. *Journal of African Earth Sciences*, **44**, 530-542. https://doi.org/10.1016/j.jafrearsci.2005.11.018

[27] Isseini, M. (2011) Croissance et différenciation crustales au Néoprotérozoïque: Exemple du domaine panafricain du Mayo-Kebbi au Sud-Ouest du Tchad. Thèse de Doctorat, Université Henri Poincaré, 339 p.

[28] Thieblemont, D. (2016) An Updated Geological Map of Africa at 1/10,000,000 Scale. *Presented at the* 35*th International Geological Congress*, Cape Town, 3 June 2016, 1-2.

[29] Genik, G.J. (1993) Petroleum Geology of Cretaceous-Tertiary Rift Basins in Niger, Chad, and Central African Republic. *AAPG Bulletin*, **77**, 1405-1434. https://doi.org/10.1306/bdff8eac-1718-11d7-8645000102c1865d

[30] Kasser, M.Y. (1998) Le précambrien tchadien: L'exemple du mayo kebbi. *Revue Scientifique du Tchad*, **5**, 51-67.

[31] Kusnir, I. and Moutaye, H.A. (1997) Ressources Minérales Du Tchad: Une Revue. *Journal of African Earth Sciences*, **24**, 549-562. https://doi.org/10.1016/s0899-5362(97)00080-8

[32] Diontar, M., Doumnang, J.C., Kwékam, M., Al-hadj Hamid, Z., Kagou Dongmo, A., Efon Awoum, J., *et al.* (2020) Petrogenesis of Magnesian High-K Granitoids from Bitkine (Centrechad Massif): Major and Trace Elements Constraints. *European Journal of Environment and Earth Sciences*, **1**, 1-5. https://doi.org/10.24018/ejgeo.2020.1.5.78

[33] Diontar, M., Kwékam, M., Fozing, E.M, Kagou, D.A. and Tcheumenak, K.J. (2020) Petrology and Geochemical Characteristic of Granitoids from Guéra Massif in the Central Part of Chad: An Example of Mixing Magmas. *Earth Science Research*, **9**, Article 66. https://doi.org/10.5539/esr.v9n2p66

[34] Shellnutt, J., Pham, N.H.T., Yeh, M.W. and Lee, T.Y. (2020) Two Series of Ediacaran Collision-Related Granites in the Guéra Massif, South-Central Chad: Tectonomagmatic Constraints on the Terminal Collision of the Eastern Central African Orogenic Belt. *Precambrian Research*, **347**, Article 105823.

[35] de Wit, M.J., Bowring, S., Buchwaldt, R., Dudas, F.Ö., MacPhee, D., Tagne-Kamga, G., *et al.* (2021) Geochemical Reconnaissance of the Guéra and Ouaddaï Massifs in Chad: Evolution of Proterozoic Crust in the Central Sahara Shield. *South African Journal of Geology*, **124**, 353-382. https://doi.org/10.25131/sajg.124.0048

[36] Shellnutt, J.G., Pham, N.H.T., Denyszyn, S.W., Yeh, M. and Lee, T. (2017) Timing of Collisional and Post-Collisional Pan-African Orogeny Silicic Magmatism in South-Central Chad. *Precambrian Research*, **301**, 113-123. https://doi.org/10.1016/j.precamres.2017.08.021

[37] Couzinié, S., Ménot, R., Doumnang, J., Paquette, J., Rochette, P., Quesnel, Y., *et al.*

(2020) Crystalline Inliers near Lake Iro (SE Chad): Post-Collisional Ediacaran A2-Type Granitic Magmatism at the Southern Margin of the Saharan Metacraton. *Journal of African Earth Sciences*, **172**, Article 103960. https://doi.org/10.1016/j.jafrearsci.2020.103960

[38] Black, R. (1992) Mission géologique au Tchad du 14/1 au 08/02/1992. Rapport InÉdit, PNUD/DRGM, 15 p.

[39] Seguem, N., Alexandre, G.A., Klötzli, U., Kepnamou, A.D. and Emmanuel, E.G. (2014) Petrography and Geochemistry of Precambrian Basement Straddling the Cameroon-Chad Border: The Touboro Baïbokoum Area. *International Journal of Geosciences*, **5**, 418-431. https://doi.org/10.4236/ijg.2014.54040

[40] Seguem, N., Diondoh, M., Kepnamou, A.D., Mama, N., Sami, M., Alexandre, G.A., *et al.* (2022) Petrography and Geochemistry of Baïbokoum-Touboro-Ngaoundaye Granitoids on the Chad-Cameroon-RCA Borders (Adamawa-Yade Domain). *Open Journal of Geology*, **12**, 136-155. https://doi.org/10.4236/ojg.2022.122007

[41] Baïssemia Ronang, G., Gountié Dedzo, M., Tcheumenak Kouémo, J., Klamadji, M.N., Mbaguedjé, D. and Kwékam, M. (2024) Petrography and Geochemical Characterization of the Baïbokoum Syenitic Pluton (Southern Chad): Implication for the Magma Genesis. *Acta Geochimica*, **44**, 420-439. https://doi.org/10.1007/s11631-024-00733-y

[42] Baïssemia, R.G., Mbaguedjé, D., Djerossem, N.F., Safianou, O., Abdoulaye, N.S., Gountié, D.M., *et al.* (2025) Incorporation of Geospatial Data and Multi-Criteria Analysis for Mapping and Assessing the Mineral Potential of the Baïbokoum Pluton (Southern Chad). *Open Journal of Geology*, **15**, 1029-1060. https://doi.org/10.4236/ojg.2025.1512054

[43] Mbaïtoudji, M.M. (1982) Lois de répartition, hypothèses de pronostics et méthodologie de la recherche des gisements de minéraux utiles solides dans le territoire de la République du Tchad. Institut de Prospection Géologique.

[44] Liégeois, J.P. (1992) Mesures des isotopes du Sr en vue de détermination d'âges des roches magmatiques du Sud du tchad (Région Baïbokoum, Léré-Figuil). Rapport inédit, 10 p.

[45] Djerossem, N.F. (2018) Croissance et remobilisation crustales au Pan-Africain dans le Sud du massif du Ouaddaï (Tchad oriental). Thèse de Doctorat, Université Toulouse-3 Paul Sabatier, 302 p.

[46] Djerossem, F., Berger, J., Vanderhaeghe, O., Isseini, M., Ganne, J. and Zeh, A. (2020) Neoproterozoic Magmatic Evolution of the Southern Ouaddaï Massif (Chad). *BSGF—Earth Sciences Bulletin*, **191**, Article 34. https://doi.org/10.1051/bsgf/2020032

[47] Pouclet, A., Vidal, M., Doumnang, J., Vicat, J. and Tchameni, R. (2006) Neoproterozoic Crustal Evolution in Southern Chad: Pan-African Ocean Basin Closing, Arc Accretion and Late- to Post-Orogenic Granitic Intrusion. *Journal of African Earth Sciences*, **44**, 543-560. https://doi.org/10.1016/j.jafrearsci.2005.11.019

[48] Isseini, M., André-Mayer, A., Vanderhaeghe, O., Barbey, P. and Deloule, E. (2012) A-Type Granites from the Pan-African Orogenic Belt in South-Western Chad Constrained Using Geochemistry, Sr-Nd Isotopes and U-Pb Geochronology. *Lithos*, **153**, 39-52. https://doi.org/10.1016/j.lithos.2012.07.014

[49] Mbaguedjé, D. (2015) Métallogénie de l'or et de l'uranium dans le cadre de la croissance et de la différenciation de la croûte au Néoprotérozoïque: Exemple du massif du mayo-kebbi (tchad) dans la ceinture orogénique d'afrique centrale. Thèse de Doctorat, Université de Lorraine, 269 p.

[50] Wacrenier, P. (1958) Carte géologique provisoire du borkou-ennedi-tibesti. Bra-

zaville, Direction de Mine et Géologie.

[51] El Makkrouf, A.A. (1988) Tectonic Interpretation of Jabal Eghei Area and Its Regional Application to Tibesti Orogenic Belt, South Central Libya. *Journal of African Earth Sciences* (*and the Middle East*), **7**, 945-967. https://doi.org/10.1016/0899-5362(88)90009-7

[52] Suayah, I.B., Miller, J.S., Miller, B.V., Bayer, T.M. and Rogers, J.J.W. (2006) Tectonic Significance of Late Neoproterozoic Granites from the Tibesti Massif in Southern Libya Inferred from Sr and Nd Isotopes and U-Pb Zircon Data. *Journal of African Earth Sciences*, **44**, 561-570. https://doi.org/10.1016/j.jafrearsci.2005.11.020

[53] De la Roche, H., Leterrier, J., Grandclaude, P. and Marchal, M. (1980) A Classification of Volcanic and Plutonic Rocks Using R1R2-Diagram and Major-Element Analyses—Its Relationships with Current Nomenclature. *Chemical Geology*, **29**, 183-210. https://doi.org/10.1016/0009-2541(80)90020-0

[54] Le Maître, R.W., Bateman, P., Dubek, A., Keller, J., Lameyre, J., Le Bas, M.J., Sabine, P.A., Schmid, R., Sorensen, H., Streckeinsen, A., Woolley, A.R. and Zanettin, B. (1989) A Classification of Igneous Rocks and Glossary of Terms. Recommendations of the International Union of Geological Sciences Sub-Commission on the Systematics of Igneous Rocks. Blackwell, 193 p.

[55] Turner, S., Arnaud, N., Liu, J., Rogers, N., Hawkesworth, C., Harris, N., *et al.* (1996) *Journal of Petrology*, **37**, 45-71. https://doi.org/10.1093/petrology/37.1.45

[56] Frost, B.R., Barnes, C.G., Collins, W.J., Arculus, R.J., Ellis, D.J. and Frost, C.D. (2001) A Geochemical Classification for Granitic Rocks. *Journal of Petrology*, **42**, 2033-2048. https://doi.org/10.1093/petrology/42.11.2033

[57] Ishikawa, Y., Sawaguchi, T., Iwaya, S. and Horiuchi, M. (1976) Delineation of Prospecting Targets for Kuroko Deposits Based on Modes of Volcanism of Underlying Dacite and Alteration Halos. *Mining Geology*, **26**, 105-117.

[58] Irvine, T.N. and Baragar, W.R.A. (1971) A Guide to the Chemical Classification of the Common Volcanic Rocks. *Canadian Journal of Earth Sciences*, **8**, 523-548. https://doi.org/10.1139/e71-055

[59] Rickwood, P.C. (1989) Boundary Lines within Petrologic Diagrams which Use Oxides of Major and Minor Elements. *Lithos*, **22**, 247-263. https://doi.org/10.1016/0024-4937(89)90028-5

[60] Sylvester, P.J. (1989) Post-Collisional Alkaline Granites. *The Journal of Geology*, **97**, 261-280. https://doi.org/10.1086/629302

[61] Maniar, P.D. and Piccoli, P.M. (1989) Tectonic Discrimination of Granitoids. *Geological Society of America Bulletin*, **101**, 635-643. https://doi.org/10.1130/0016-7606(1989)101<0635:tdog>2.3.co;2

[62] Harker, A. (1909) The Natural History of Igneous Rocks. Methuen.

[63] Irber, W. (1999) The Lanthanide Tetrad Effect and Its Correlation with K/Rb, EuN/Eu*, Sr/Eu, Y/Ho, and Zr/Hf of Evolving Peraluminous Granite Suites. *Geochimica et Cosmochimica Acta*, **63**, 489-508. https://doi.org/10.1016/s0016-7037(99)00027-7

[64] Sun, S. and McDonough, W.F. (1989) Chemical and Isotopic Systematics of Oceanic Basalts: Implications for Mantle Composition and Processes. *Geological Society, London, Special Publications*, **42**, 313-345. https://doi.org/10.1144/gsl.sp.1989.042.01.19

[65] Taylor, S.R. and McLennan, S.M. (1985) The Continental Crust: Its Composition and Evolution. Blackwell Scientific Publication, 312 p.

[66] Kelemen, P.B., Johnson, K.T.M., Kinzler, R.J. and Irving, A.J. (1990) High-Field-

Strength Element Depletions in Arc Basalts Due to Mantle-Magma Interaction. *Nature*, **345**, 521-524. https://doi.org/10.1038/345521a0

[67] Brown, G.C., Thorpe, R.S. and Webb, P.C. (1984) The Geochemical Characteristics of Granitoids in Contrasting Arcs and Comments on Magma Sources. *Journal of the Geological Society*, **141**, 413-426. https://doi.org/10.1144/gsjgs.141.3.0413

[68] Boynton, W.V. (1984) Cosmochemistry of the Rare Earth Elements: Meteorite Studies. In: Henderson, P., Ed., *Developments in Geochemistry*, Elsevier, 63-114. https://doi.org/10.1016/b978-0-444-42148-7.50008-3

[69] Basua, A.A.E., Ma, C., Nguo, K.S., Wang, L., Lentz, D.R., Mukherjee, S., *et al.* (2022) Petrogenesis and Tectonic Setting of A-Type Granites in the Babouri-Figuil Magmatic Complex (North Cameroon): Constraints from Whole Rock Geochemistry, Zircon U-Pb Geochronology and Sr-Nd-Hf Isotopes. *Lithos*, **414**, Article 106618. https://doi.org/10.1016/j.lithos.2022.106618

[70] Wilson, M. (1989) Igneous Petrogenesis. Unwin-Hyman, 456 p.

[71] MacLean, W.H. (1990) Mass Change Calculations in Altered Rock Series. *Mineralium Deposita*, **25**, 44-49. https://doi.org/10.1007/bf03326382

[72] Münker, C., Wörner, G., Yogodzinski, G. and Churikova, T. (2004) Behaviour of High Field Strength Elements in Subduction Zones: Constraints from Kamchatka-Aleutian Arc Lavas. *Earth and Planetary Science Letters*, **224**, 275-293. https://doi.org/10.1016/j.epsl.2004.05.030

[73] Polat, A. and Hofmann, A.W. (2003) Alteration and Geochemical Patterns in the 3.7-3.8 Ga Isua Greenstone Belt, West Greenland. *Precambrian Research*, **126**, 197-218. https://doi.org/10.1016/s0301-9268(03)00095-0

[74] Spitz, G. and Darling, R. (1978) Major and Minor Element Lithogeochemical Anomalies Surrounding the Louvem Copper Deposit, Val D'or, Quebec. *Canadian Journal of Earth Sciences*, **15**, 1161-1169. https://doi.org/10.1139/e78-122

[75] Large, R.R., Gemmell, J.B. and Paulick, H. (2001) The Alteration Box Plot: A Simple Approach to Understanding the Relationship between Alteration Mineralogy and Lithogeochemistry Associated with Volcanic-Hosted Massive Sulfide Deposits. *Economic Geology*, **96**, 957-971. https://doi.org/10.2113/96.5.957

[76] Pearce, J.A., Kempton, P.D., Nowell, G.M. and Noble, S.R. (1999) HF-Nd Element and Isotope Perspective on the Nature and Provenance of Mantle and Subduction Components in Western Pacific Arc-Basin Systems. *Journal of Petrology*, **40**, 1579-1611. https://doi.org/10.1093/petroj/40.11.1579

[77] Schandl, E.S. and Gorton, M.P. (2002) Application of High Field Strength Elements to Discriminate Tectonic Settings in VMS Environments. *Economic Geology*, **97**, 629-642. https://doi.org/10.2113/gsecongeo.97.3.629

[78] Shellnutt, J.G., Yeh, M., Lee, T., Iizuka, Y., Pham, N.H.T. and Yang, C. (2018) The Origin of Late Ediacaran Post-Collisional Granites Near the Chad Lineament, Saharan Metacraton, South-Central Chad. *Lithos*, **304**, 450-467. https://doi.org/10.1016/j.lithos.2018.02.020

[79] Whalen, J.B., Currie, K.L. and Chappell, B.W. (1987) A-Type Granites: Geochemical Characteristics, Discrimination and Petrogenesis. *Contributions to Mineralogy and Petrology*, **95**, 407-419. https://doi.org/10.1007/bf00402202

[80] Pitcher, W.S. (1993) The Nature and Origin of Granite. Blackie Academic and Professional, 321 p.

[81] Chappell, B.W., Bryant, C.J. and Wyborn, D. (2012) Peraluminous I-Type Granites. *Lithos*, **153**, 142-153. https://doi.org/10.1016/j.lithos.2012.07.008

[82] Dong, Y., Ge, W., Tian, D., Ji, Z., Yang, H., Bi, J., *et al.* (2019) Geochronology and Geochemistry of Early Cretaceous Granitic Plutons in the Xing'an Massif, Great Xing'an Range, NE China: Petrogenesis and Tectonic Implications. *Acta Geologica Sinica-English Edition*, **93**, 1500-1521. https://doi.org/10.1111/1755-6724.14391

[83] Miller, C.F. (1985) Are Strongly Peraluminous Magmas Derived from Pelitic Sedimentary Sources? *The Journal of Geology*, **93**, 673-689. https://doi.org/10.1086/628995

[84] Clemens, J.D. (2018) Granitic Magmas with I-Type Affinities, from Mainly Metasedimentary Sources: The Harcourt Batholith of Southeastern Australia. *Contributions to Mineralogy and Petrology*, **173**, Article No. 93. https://doi.org/10.1007/s00410-018-1520-z

[85] Chappell, B.W. (1999) Aluminium Saturation in I- and S-Type Granites and the Characterization of Fractionated Haplogranites. *Lithos*, **46**, 535-551. https://doi.org/10.1016/s0024-4937(98)00086-3

[86] Wu, F.Y., Li, X.H., Zheng, Y.F. and Gao, S. (2007) Lu-Hf Isotopic Systematics and Their Applications in Petrology. *Acta Petrologica Sinica*, **23**, 185-220.

[87] Li, H., Palinkaš, L.A., Watanabe, K. and Xi, X. (2018) Petrogenesis of Jurassic A-Type Granites Associated with Cu-Mo and W-Sn Deposits in the Central Nanling Region, South China: Relation to Mantle Upwelling and Intra-Continental Extension. *Ore Geology Reviews*, **92**, 449-462. https://doi.org/10.1016/j.oregeorev.2017.11.029

[88] Eby, G.N. (1992) Chemical Subdivision of the A-Type Granitoids: Petrogenetic and Tectonic Implications. *Geology*, **20**, 641-644. https://doi.org/10.1130/0091-7613(1992)020<0641:csotat>2.3.co;2

[89] Ma, C., She, Z., Xu, P. and Wang, L. (2005) Silurian A-Type Granitoids in the Southern Margin of the Tongbai-Dabieshan: Evidence from SHRIMP Zircon Geochronology and Geochemistry. *Science in China Series D*: *Earth Sciences*, **48**, 1134-1145. https://doi.org/10.1360/03yd0487

[90] Bonin, B. (2007) A-Type Granites and Related Rocks: Evolution of a Concept, Problems and Prospects. *Lithos*, **97**, 1-29. https://doi.org/10.1016/j.lithos.2006.12.007

[91] Foley, S.F., Barth, M.G. and Jenner, G.A. (2000) Rutile/Melt Partition Coefficients for Trace Elements and an Assessment of the Influence of Rutile on the Trace Element Characteristics of Subduction Zone Magmas. *Geochimica et Cosmochimica Acta*, **64**, 933-938. https://doi.org/10.1016/s0016-7037(99)00355-5

[92] Clemens, J. (2003) S-Type Granitic Magmas—Petrogenetic Issues, Models and Evidence. *Earth-Science Reviews*, **61**, 1-18. https://doi.org/10.1016/s0012-8252(02)00107-1

[93] Defant, M.J. and Drummond, M.S. (1990) Derivation of Some Modern Arc Magmas by Melting of Young Subducted Lithosphere. *Nature*, **347**, 662-665. https://doi.org/10.1038/347662a0

[94] Dall'Agnol, R. and de Oliveira, D.C. (2007) Oxidized, Magnetite-Series, Rapakivi-Type Granites of Carajás, Brazil: Implications for Classification and Petrogenesis of A-Type Granites. *Lithos*, **93**, 215-233. https://doi.org/10.1016/j.lithos.2006.03.065

[95] Loiselle, M.C. and Wones, D. (1979) Characteristics and Origin of Anorogenic Granites. *Abstracts with Programs—Geological Society of America*, **11**, Article 468.

[96] Beyth, M., Stern, R.J., Altherr, R. and Kröner, A. (1994) The Late Precambrian Timna Igneous Complex, Southern Israel: Evidence for Comagmatic-Type Sanukitoid Monzodiorite and Alkali Granite Magma. *Lithos*, **31**, 103-124. https://doi.org/10.1016/0024-4937(94)90003-5

[97] Clemens, J.D., Holloway, J.R. and White, A.J.R. (1986) Origin of an A-Type Granite;

Experimental Constraints. *American Mineralogist*, **71**, 317-324.

[98] Eby, G.N. (1990) The A-Type Granitoids: A Review of Their Occurrence and Chemical Characteristics and Speculations on Their Petrogenesis. *Lithos*, **26**, 115-134. https://doi.org/10.1016/0024-4937(90)90043-z

[99] Frost, C.D. and Frost, B.R. (2010) On Ferroan (A-Type) Granitoids: Their Compositional Variability and Modes of Origin. *Journal of Petrology*, **52**, 39-53. https://doi.org/10.1093/petrology/egq070

[100] Breiter, K. (2012) Nearly Contemporaneous Evolution of the A- and S-Type Fractionated Granites in the Krušné Hory/Erzgebirge Mts., Central Europe. *Lithos*, **151**, 105-121. https://doi.org/10.1016/j.lithos.2011.09.022

[101] Hofmann, A.W. (1988) Chemical Differentiation of the Earth: The Relationship between Mantle, Continental Crust, and Oceanic Crust. *Earth and Planetary Science Letters*, **90**, 297-314. https://doi.org/10.1016/0012-821x(88)90132-x

[102] Rudnick, R.L. and Fountain, D.M. (1995) Nature and Composition of the Continental Crust: A Lower Crustal Perspective. *Reviews of Geophysics*, **33**, 267-309. https://doi.org/10.1029/95rg01302

[103] Weaver, B.L. and Tarney, J. (1984) Empirical Approach to Estimating the Composition of the Continental Crust. *Nature*, **310**, 575-577. https://doi.org/10.1038/310575a0

[104] Vernon, R.H. (1984) Microgranitoid Enclaves in Granites—Globules of Hybrid Magma Quenched in a Plutonic Environment. *Nature*, **309**, 438-439. https://doi.org/10.1038/309438a0

[105] Tang, M., Wang, X., Shu, X., Wang, D., Yang, T. and Gopon, P. (2014) Hafnium Isotopic Heterogeneity in Zircons from Granitic Rocks: Geochemical Evaluation and Modeling of "Zircon Effect" in Crustal Anatexis. *Earth and Planetary Science Letters*, **389**, 188-199. https://doi.org/10.1016/j.epsl.2013.12.036

[106] Plank, T. (2005) Constraints from Thorium/Lanthanum on Sediment Recycling at Subduction Zones and the Evolution of the Continents. *Journal of Petrology*, **46**, 921-944. https://doi.org/10.1093/petrology/egi005

[107] Hayashi, K., Fujisawa, H., Holland, H.D. and Ohmoto, H. (1997) Geochemistry of ~1.9 Ga Sedimentary Rocks from Northeastern Labrador, Canada. *Geochimica et Cosmochimica Acta*, **61**, 4115-4137. https://doi.org/10.1016/s0016-7037(97)00214-7

[108] Laurent, O., Martin, H., Moyen, J.F. and Doucelance, R. (2014) The Diversity and Evolution of Late-Archean Granitoids: Evidence for the Onset of "Modern-Style" Plate Tectonics between 3.0 and 2.5Ga. *Lithos*, **205**, 208-235. https://doi.org/10.1016/j.lithos.2014.06.012

[109] Altherr, R., Holl, A., Hegner, E., Langer, C. and Kreuzer, H. (2000) High-Potassium, Calc-Alkaline I-Type Plutonism in the European Variscides: Northern Vosges (France) and Northern Schwarzwald (Germany). *Lithos*, **50**, 51-73. https://doi.org/10.1016/s0024-4937(99)00052-3

[110] Jung, S. and Pfänder, J.A. (2007) Source Composition and Melting Temperatures of Orogenic Granitoids: Constraints from CaO/Na_2O, Al_2O_3/TiO_2 and Accessory Mineral Saturation Thermometry. *European Journal of Mineralogy*, **19**, 859-870. https://doi.org/10.1127/0935-1221/2007/0019-1774

[111] Sylvester, P.J. (1998) Post-Collisional Strongly Peraluminous Granites. *Lithos*, **45**, 29-44. https://doi.org/10.1016/s0024-4937(98)00024-3

[112] Furman, T. and Graham, D. (1999) Erosion of Lithospheric Mantle beneath the East African Rift System: Geochemical Evidence from the Kivu Volcanic Province. *Lithos*,

48, 237-262. https://doi.org/10.1016/s0024-4937(99)00031-6

[113] Zhu, Y., Lai, S., Qin, J., Zhu, R., Zhang, F. and Zhang, Z. (2020) Petrogenesis and Geochemical Diversity of Late Mesoproterozoic S-Type Granites in the Western Yangtze Block, South China: Co-Entrainment of Peritectic Selective Phases and Accessory Minerals. *Lithos*, **352**, 105326. https://doi.org/10.1016/j.lithos.2019.105326

[114] Conway, C.M., Condie, K.C. and Noll, P.D. (1993) Geochemical and Detrital Mode Evidence for Two Sources of Early Proterozoic Sedimentary Rocks from the Tonto Basin Supergroup, Central Arizona—Reply. *Sedimentary Geology*, **87**, 241-244. https://doi.org/10.1016/0037-0738(93)90007-r

[115] Moreno, J.A., Molina, J.F., Montero, P., Abu Anbar, M., Scarrow, J.H., Cambeses, A., *et al.* (2014) Unraveling Sources of A-Type Magmas in Juvenile Continental Crust: Constraints from Compositionally Diverse Ediacaran Post-Collisional Granitoids in the Katerina Ring Complex, Southern Sinai, Egypt. *Lithos*, **192**, 56-85. https://doi.org/10.1016/j.lithos.2014.01.010

[116] Deyhimi, M., Kananian, A., Mirnejad, H., Sepidbar, F., Vlastelic, I., Paquette, J., *et al.* (2019) Zircon U-Pb Geochronology, Major-Trace Elements and Sr-Nd Isotope Geochemistry of Mashhad Granodiorites (NE Iran) and Their Mafic Microgranular Enclaves: Evidence for Magma Mixing and Mingling. *International Geology Review*, **62**, 1615-1634. https://doi.org/10.1080/00206814.2019.1600435

[117] Harris, N.B.W. and Inger, S. (1992) Trace Element Modelling of Pelite-Derived Granites. *Contributions to Mineralogy and Petrology*, **110**, 46-56. https://doi.org/10.1007/bf00310881

[118] McDermott, F., Harris, N.B.W. and Hawkesworth, C.J. (1996) Geochemical Constraints on Crustal Anatexis: A Case Study from the Pan-African Damara Granitoids of Namibia. *Contributions to Mineralogy and Petrology*, **123**, 406-423. https://doi.org/10.1007/s004100050165

[119] Barbarin, B. (1996) Genesis of the Two Main Types of Peraluminous Granitoids. *Geology*, **24**, 295-298. https://doi.org/10.1130/0091-7613(1996)024<0295:gottmt>2.3.co;2

[120] Watt, G.R. and Harley, S.L. (1993) Accessory Phase Controls on the Geochemistry of Crustal Melts and Restites Produced during Water-Undersaturated Partial Melting. *Contributions to Mineralogy and Petrology*, **114**, 550-566. https://doi.org/10.1007/bf00321759

[121] Zheng, Z., Chen, Y., Deng, X., Yue, S., Chen, H. and Wang, Q. (2018) Origin of the Bashierxi Monzogranite, Qiman Tagh, East Kunlun Orogen, NW China: A Magmatic Response to the Evolution of the Proto-Tethys Ocean. *Lithos*, **296**, 181-194. https://doi.org/10.1016/j.lithos.2017.10.019

[122] Achu Megnemo, L., Fozing, E.M., Tcheumenak Kouémo, J., Efon Awoum, J., Sobze Yemdji, R.B., Aman, S.L., *et al.* (2026) Upper-Crustal Emplacement Mode of the Neoproterozoic Ngwi Granites along the Central Cameroon Shear Zone, Adamawa-Yadé Domain, West-Central Cameroon: Implications for Regional Tectonic Control. *Acta Geologica Sinica-English Edition*, **100**, 325-347. https://doi.org/10.1111/1755-6724.70028

[123] Shellnutt, G., Yeh, M., Pham, N.H. and Lee, T. (2021) Late Ediacaran Post-Collisional Magmatism in the Guéra Massif, South-Central Chad. *International Geology Review*, **64**, 1097-1118. https://doi.org/10.7185/gold2021.3212

[124] Clemens, J.D. and Stevens, G. (2012) What Controls Chemical Variation in Granitic Magmas? *Lithos*, **134**, 317-329. https://doi.org/10.1016/j.lithos.2012.01.001

[125] Healy, B., Collins, W.J. and Richards, S.W. (2004) A Hybrid Origin for Lachlan S-Type Granites: The Murrumbidgee Batholith Example. *Lithos*, **78**, 197-216.

https://doi.org/10.1016/j.lithos.2004.04.047

[126] Foden, J.D., Elburg, M.A., Turner, S.P., Sandiford, M., O'Callaghan, J. and Mitchell, S. (2002) Granite Production in the Delamerian Orogen, South Australia. *Journal of the Geological Society*, **159**, 557-575. https://doi.org/10.1144/0016-764901-099

[127] Zhao, Z., Gao, P. and Zheng, Y. (2015) The Source of Mesozoic Granitoids in South China: Integrated Geochemical Constraints from the Taoshan Batholith in the Nanling Range. *Chemical Geology*, **395**, 11-26. https://doi.org/10.1016/j.chemgeo.2014.11.028

[128] Wu, T., Xiao, L., Wilde, S.A., Ma, C. and Zhou, J. (2017) *Lithos*, **288**, 214-230. https://doi.org/10.1016/j.lithos.2017.07.002

[129] Cocherie, A. (1986) Systematic Use of Trace Element Distribution Patterns in Log-Log Diagrams for Plutonic Suites. *Geochimica et Cosmochimica Acta*, **50**, 2517-2522. https://doi.org/10.1016/0016-7037(86)90034-7

[130] Moghazi, A.M. (2002) Petrology and Geochemistry of Pan-African Granitoids, Kab Amiri Area, Egypt-Implications for Tectonomagmatic Stages in the Nubian Shield Evolution. *Mineralogy and Petrology*, **75**, 41-67. https://doi.org/10.1007/s007100200014

[131] Allègre, C.J. and Minster, J.F. (1978) Quantitative Models of Trace Element Behavior in Magmatic Processes. *Earth and Planetary Science Letters*, **38**, 1-25. https://doi.org/10.1016/0012-821x(78)90123-1

[132] Breaks, F.W. and Moore, J.M. (1992) The Ghost Lake Batholith, Superior Province of North-Western Ontario: A Fertile, S-Type, Peraluminous Granite-Rare Element Pegmatite System. *The Canadian Mineralogist*, **30**, 835-876.

[133] Watson, E.B. and Harrison, T.M. (1983) Zircon Saturation Revisited: Temperature and Composition Effects in a Variety of Crustal Magma Types. *Earth and Planetary Science Letters*, **64**, 295-304. https://doi.org/10.1016/0012-821x(83)90211-x

[134] Boehnke, P., Watson, E.B., Trail, D., Harrison, T.M. and Schmitt, A.K. (2013) Zircon Saturation Re-Revisited. *Chemical Geology*, **351**, 324-334. https://doi.org/10.1016/j.chemgeo.2013.05.028

[135] Winkler, H.G.F., Boese, M. and Marcopoulos, T. (1975) Low Temperature Granitic Melts. *Neues Jahrbuch für Mineralogie Monatsh*, **6**, 245-268.

[136] Siégel, C., Bryan, S.E., Allen, C.M. and Gust, D.A. (2018) Use and Abuse of Zircon-Based Thermometers: A Critical Review and a Recommended Approach to Identify Antecrystic Zircons. *Earth-Science Reviews*, **176**, 87-116. https://doi.org/10.1016/j.earscirev.2017.08.011

[137] Pearce, J.A., Harris, N.B.W. and Tindle, A.G. (1984) Trace Element Discrimination Diagrams for the Tectonic Interpretation of Granitic Rocks. *Journal of Petrology*, **25**, 956-983. https://doi.org/10.1093/petrology/25.4.956

[138] Pearce, J. (1996) Sources and Settings of Granitic Rocks. *Episodes*, **19**, 120-125. https://doi.org/10.18814/epiiugs/1996/v19i4/005

[139] Whalen, J.B. and Hildebrand, R.S. (2019) Trace Element Discrimination of Arc, Slab Failure, and A-Type Granitic Rocks. *Lithos*, **348**, Article 105179. https://doi.org/10.1016/j.lithos.2019.105179

[140] Müller, D. and Groves, D.I. (1997) Potassic Igneous Rocks and Associated Gold-Copper Mineralization. 3rd Edition, Springer, 238 p.

[141] Roberts, M.P. and Clemens, J.D. (1993) Origin of High-Potassium, Talc-Alkaline, I-Type Granitoids. *Geology*, **21**, 825-828. https://doi.org/10.1130/0091-7613(1993)021<0825:oohpta>2.3.co;2

[142] Janoušek, V., Farrow, C.M. and Erban, V. (2006) Interpretation of Whole-Rock Geochemical Data in Igneous Geochemistry: Introducing Geochemical Data Toolkit (Gcdkit). *Journal of Petrology*, **47**, 1255-1259. https://doi.org/10.1093/petrology/egl013

[143] Pham, C.T., Shellnutt, J.G., Yeh, M. and Iizuka, Y. (2020) An Assessment of the Magmatic Conditions of Late Neoproterozoic Collisional and Post-Collisional Granites from the Guéra Massif, South-Central Chad. *Frontiers in Earth Science*, **8**, Article ID: 318. https://doi.org/10.3389/feart.2020.00318

[144] Liégeois, J.P., Black, R., Navez, J. and Latouche, L. (1994) Early and Late Pan-African Orogenies in the Aïr Assembly of Terranes (Tuareg Shield, Niger). *Precambrian Research*, **67**, 59-88. https://doi.org/10.1016/0301-9268(94)90005-1

[145] Higgins, M.D. (2017) Quantitative Investigation of Felsic Rock Textures Using Cathodoluminescence Images and Other Techniques. *Lithos*, **277**, 259-268. https://doi.org/10.1016/j.lithos.2016.05.006

[146] Christiansen, E.H. and Keith, J.D. (1996) Trace Element Systematics in Silicic Magmas: A Metallogenic Perspective. In: *Trace Element Geochemistry of Volcanic Rocks: Applications for Massive Sulfde Exploration*, Geological Association of Canada, Short Course Notes, Vol. 12, 115-151.

[147] Houketchang Bouyo, M., Penaye, J., Njel, U.O., Moussango, A.P.I., Sep, J.P.N., Nyama, B.A., *et al.* (2016) Geochronological, Geochemical and Mineralogical Constraints of Emplacement Depth of TTG Suite from the Sinassi Batholith in the Central African Fold Belt (CAFB) of Northern Cameroon: Implications for Tectonomagmatic Evolution. *Journal of African Earth Sciences*, **116**, 9-41. https://doi.org/10.1016/j.jafrearsci.2015.12.005

[148] Nomo, E.N., Tchameni, R., Vanderhaeghe, O., Sun, F., Barbey, P., Tekoum, L., *et al.* (2017) Structure and LA-ICP-MS Zircon U-Pb Dating of Syntectonic Plutons Emplaced in the Pan-African Banyo-Tcholliré Shear Zone (Central North Cameroon). *Journal of African Earth Sciences*, **131**, 251-271. https://doi.org/10.1016/j.jafrearsci.2017.04.002

[149] Tiani Djuimou, S., Bouyo Houketchang, M., Vanderhaeghe, O., Achu Megnemo, L., Azefack Mbounou, L.R., Gregoire, M., *et al.* (2025) The Djourdé-Sinassi Magmatic-Migmatitic Complex, Northern Cameroon: A Record of Vertical Extrusion of the Pan-African Partially Molten Orogenic Root. *BSGF-Earth Sciences Bulletin*, **196**, Article 11. https://doi.org/10.1051/bsgf/2025014

[150] Shellnutt, J.G., Yeh, M., Pham, N.H.T. and Lee, T. (2019) Cryptic Regional Magmatism in the Southern Saharan Metacraton at 580 Ma. *Precambrian Research*, **332**, Article 105398. https://doi.org/10.1016/j.precamres.2019.105398

[151] Pham, T.N.H. (2018) Timing and Petrogenesis of Collisional and Post-Collisional Rocks of Guéra Massif, Republic of Chad. Master's Thesis, NTNU.

[152] Mahamat Boka, R., Baïssemia Ronang, G., Doumnang Mbaïgane, J.C., Madjimbe G. and Allarassem, L., (2025) Romote Sensing Mapping of the Basement Rocks of Northern Korbol in Moyen Chari Province, Southern Chad. *Asian Journal of Science and Technology*, **16**, 13933-13940.

[153] Sobh, M., Ebbing, J., Mansi, A.H., Götze, H., Emry, E.L. and Abdelsalam, M.G. (2020) The Lithospheric Structure of the Saharan Metacraton from 3-D Integrated Geophysical-Petrological Modeling. *Journal of Geophysical Research: Solid Earth*, **125**, e2019JB018747. https://doi.org/10.1029/2019jb018747